Experiments quantifying elemental and isotopic fractionations during evaporation of CAI-like melts in low-pressure hydrogen and in vacuum: Constraints on thermal processing of CAI in the protoplanetary disk

Ruslan A. Mendybaev[1], Michiru Kamibayashi[2,3], Fang-Zhen Teng[4], Paul S. Savage[5], R. Bastian Georg[6], Frank M. Richter[1] and Shogo Tachibana[2,3,7]

[1] Department of the Geophysical Sciences, University of Chicago, Chicago, IL 60637
[2] Department of Natural History Sciences, Hokkaido University, Sapporo 060-0810, Japan
[3] Department of Earth and Planetary Sciences, University of Tokyo, Tokyo 113-0033, Japan
[4] Department of Earth and Space Sciences, University of Washington, Seattle, WA 98195
[5] School of Earth and Environmental Sciences, University of St. Andrews, St. Andrews, KY16 9AL, Scotland
[6*] Water Quality Center, Trent University, Peterborough, ON K9L0G2, Canada
[7] Institute of Space and Astronautical Science, JAXA, Tokyo 252-0222, Japan

[*]Now at: Agilent Technologies, Mississauga, ON L5N 5M4, Canada.

Corresponding author: Ruslan A. Mendybaev (ramendyb@uchicago.edu)

Submitted to *Geochimica et Cosmochimica Acta*

April 5, 2020

Revised: 9-3-2020

ABSTRACT

It is widely believed that the precursors of coarse-grained CAIs in chondrites are solar nebula condensates that were later reheated and melted to a high degree. Such melting under low-pressure conditions is expected to result in evaporation of moderately volatile magnesium and silicon and their mass-dependent isotopic fractionation. The evaporation of silicate melts has been extensively studied in vacuum laboratory experiments and a large experimental database on chemical and isotopic fractionations now exists. Nevertheless, it remains unclear if vacuum evaporation of CAI-like melts adequately describes the evaporation in the hydrogen-rich gas of the solar nebula. Here we report the results of a detailed experimental study on evaporation of a such melt at 1600°C in both vacuum and low-pressure hydrogen gas, using 1.5- and 2.5-mm diameter samples. The experiments show that although at 2×10^{-4} bar H_2 magnesium and silicon evaporate ~2.8 times faster than at 2×10^{-5} bar H_2 and ~45 times faster than in vacuum, their relative evaporation rates and isotopic fractionation factors remain the same. This means that the chemical and isotopic evolutions of all evaporation residues plot along a single evaporation trajectory regardless of experimental conditions (vacuum or low-P_{H_2}) and sample size. The independence of chemical and isotopic evaporation trajectories on P_{H_2} of the surrounding gas imply that the existing extensive experimental database on vacuum evaporation of CAI-like materials can be safely used to model the evaporation under solar nebula conditions, taking into account the dependence of evaporation kinetics on P_{H_2}.

The experimental data suggest that it would take less than 25 minutes at 1600°C to evaporate 15–50% of magnesium and 5–20% of silicon from a 2.5-mm diameter sample in a solar nebula with P_{H_2}~2×10^{-4} bar and to enrich the residual melt in heavy magnesium and silicon isotopes up to δ^{25}Mg ~ 5–10‰ and δ^{29}Si ~ 2–4‰. The expected chemical and isotopic features are compatible to those typically observed in coarse-grained Type A and B CAIs. Evaporation for ~1 hour will produce δ^{25}Mg ~30–35‰ and δ^{29}Si ~10–15‰, close to the values in highly fractionated Type F and FUN CAIs. These very short timescales suggest melting and evaporation of CAI precursors in very short dynamic heating events. The experimental results reported here provide a stringent test of proposed astrophysical models for the origin and evolution of CAIs.

Keywords

CAI evaporation; Experiments; Kinetics; Elemental fractionation; Isotopic fractionation; Magnesium; Silicon; Timescales; Astrophysical models; Nebular shock.

1. INTRODUCTION

Formation and pre-accretional thermal processing of Ca-Al-rich inclusions (CAIs) - the oldest known material of the solar system (e.g., Amelin et al., 2010; Bouvier and Wadhwa, 2010; Connelly et al., 2012) - remains a major unsolved problem in cosmochemistry. Although recent advances in analytical instrumentation have generated a large volume information on the mineralogy and chemical and isotopic compositions of CAIs (see reviews of MacPherson, 2014 and Krot, 2019 and references therein), which has greatly improved our understanding of the formation and evolution of these early solar system materials, the quantitative interpretation of these data still requires their experimental calibration under conditions close to those of the natural systems.

Coarse-grained igneous textures of "normal" Type B and Compact Type A CAI, and FUN (with isotopic **F**ractionation and **U**nidentified **N**uclear anomalies) and Type F (with isotopic **F**ractionation) CAIs suggest that such CAIs have experienced at least one high-temperature melting event followed by slow cooling at a rate of less than 50°C per hour (e.g., MacPherson et al., 1984; Stolper and Paque, 1986; Mendybaev et al., 2006a). If the melting of precursor silicate material of CAIs occurred under low-pressure conditions, one would expect the evaporative loss of moderately volatile elements (e.g., Mg, Si, and O), which would result in chemical and mass-dependent isotopic fractionations due to the different element volatilities and relatively faster evaporation of the lighter isotopes (e.g., Richter et al., 2002; 2007). The coarse-grained CAIs are often characterized by the depletion of Mg and Si relative to compositions expected from condensation of solar nebula gas. Coarse-grained CAIs also display correlated enrichments in heavy Mg and Si isotopes of up to δ^{25}Mg ~ 35‰ and δ^{29}Si ~ 17‰, such as in Allende FUN CAI CMS-1 (Williams et al., 2017), indicating that high-temperature melting and evaporation of molten droplets occurred at early stages of formation and evolution of solar system materials.

To better understand the physicochemical processes that resulted in the formation of CAIs and to provide a basis for quantitative interpretation of the available analytical data, a large number of high-temperature vacuum evaporation experiments have been conducted using CAI-like CaO-MgO-Al_2O_3-SiO_2 (CMAS) melts (e.g., Davis et al., 1990; Floss et al., 1996; Wang et al., 2001; Richter et al., 2002; 2007; Knight et al., 2009; Mendybaev and Richter, 2016; Mendybaev et al., 2013a; 2017). Such experiments have determined the evaporation kinetics of Mg, Si and O from different CMAS melts, as well as the evolution of the chemical and isotopic compositions during evaporation as a function of temperature. The Mg-, Si-, and O-isotopic fractionation factors obtained in these experiments have subsequently been used to reconstruct precursor compositions of the CAIs (e.g., Grossman et al., 2000; Knight et al., 2009; Mendybaev et al., 2013a; 2017).

However, the question remains as to whether the existing database on chemical and isotopic fractionation derived from vacuum evaporation experiments adequately describes the evaporation in the hydrogen-rich gas of the solar nebula. To date, the only experimental investigation of evaporation of CAI-like melts under low-P_{H_2} conditions is limited to a few experiments by Richter et al. (2002) who evaporated Type B CAI-like melt at 1500ºC and $P_{H_2}=2\times10^{-4}$ bar. They found that 30 to 240 minutes of evaporation resulted in loss of Mg of up to ~91% with corresponding δ^{25}Mg fractionation of up to ~31‰. The measured evaporation rates in

these low-P_{H_2} experiments were estimated to be two orders of magnitude faster than if the same composition melt would have evaporated at 1500°C in a vacuum. The direct comparison of evaporation kinetics and chemical and isotopic fractionations in low-pressure H_2 solar nebula environment and in vacuum is limited by very slow evaporation kinetics of CMAS melts at 1500°C in vacuum: it would take several weeks to months to evaporate significant amount of magnesium and silicon. In this paper we will present results of new laboratory evaporation experiments in vacuum and low-P_{H_2} conditions, conducted at 1600°C, using the same starting CAI-like material. The purpose of the experiments was to determine whether evaporation under different low-pressure conditions (vacuum, ~2×10^{-5} bar H_2 and ~2×10^{-4} bar H_2) would affect evaporation kinetics, and elemental and Mg and Si isotopic fractionations.

2. THEORETICAL FRAMEWORK

The theoretical framework of the evaporation processes has been described in detail by Richter et al. (2002, 2007) and below we review some aspects related to the evaporation of CMAS liquids relevant to this study.

Evaporation of silicate melts in a vacuum can be described by the standard Hertz-Knudsen-Langmuir equation (Hirth and Pound, 1963):

$$J_{i,net} = \sum_{j=1}^{n} \frac{n_{ij}\gamma_{ij}(P_{ij,sat}-P_{ij})}{\sqrt{2\pi m_{ij}RT}} \quad (1)$$

where $J_{i,net}$ is the net evaporative flux of a component i (element or isotope), n_{ij} is the number of atoms of i in the jth gas species containing i, γ_{ij} is the evaporation coefficient for the jth gas species containing i, $P_{ij,sat}$ and P_{ij} are the saturation vapor pressure and pressure of j at the melt-gas interface, m_{ij} is the molar mass of the gas species j that would be in equilibrium with the melt, R is the gas constant, and T is the absolute temperature. Under low-pressure conditions, P_{ij} becomes negligible and in case of Mg and Si evaporating from CMAS melts, the Eq. (1) can be simplified to:

$$J_{Mg} = \frac{\gamma_{Mg}P_{Mg,sat}}{\sqrt{2\pi m_{Mg}RT}} \quad (2)$$

and

$$J_{SiO} = \frac{\gamma_{SiO}P_{SiO,sat}}{\sqrt{2\pi m_{SiO}RT}}, \quad (3)$$

where J_{Mg} and J_{SiO} are the evaporative fluxes of magnesium and silicon, γ_{Mg} and γ_{SiO} are the empirical evaporation coefficients of $Mg_{(g)}$ and $SiO_{(g)}$, $P_{Mg,sat}$ and $P_{SiO,sat}$ are their vapor pressures in equilibrium with the melt, m_{Mg} and m_{SiO} are their molar masses. J_{Mg} and J_{SiO} are essentially the total evaporation rates of magnesium and silicon, since $Mg_{(g)}$ and $SiO_{(g)}$ are dominant gaseous species of Mg and Si in equilibrium with high-temperature silicate melts according to thermodynamic calculations (e.g., Grossman et al., 2000) and Knudsen cell measurements (e.g., Shornikov and Yakovlev, 2015; Costa et al., 2017 and references therein). The relative evaporation rates of magnesium and silicon then are:

$$\frac{J_{Si}}{J_{Mg}} = \frac{\gamma_{SiO}}{\gamma_{Mg}}\frac{P_{SiO,sat}}{P_{Mg,sat}}\sqrt{\frac{m_{Mg}}{m_{SiO}}}, \quad (4)$$

and can be calculated if the evaporation coefficients γ_{Mg} and γ_{SiO} and equilibrium vapor pressures P_{Mg} and P_{SiO} are known. Since only Si and Mg evaporate from a CAI-like CMAS melt (refractory Ca and Al remain in the melt until near-complete evaporation of Mg and Si), it is the ratio J_{Mg}/J_{Si} that determines how the chemical composition of such melts evolve during evaporation.

Extending Eq. (4), if the element *i* evaporates predominantly as a single gas species, the ratio of the fluxes of isotopes *1* and *2* of a given element *i* can be expressed as:

$$\frac{J_{i,2}}{J_{i,1}} = \frac{\gamma_{i,2}}{\gamma_{i,1}}\frac{P_{i,2}}{P_{i,1}}\sqrt{\frac{m_{i,1}}{m_{i,2}}} = R_{2,1}\frac{\gamma_{i,2}}{\gamma_{i,1}}\sqrt{\frac{m_{i,1}}{m_{i,2}}} \quad (5)$$

where $R_{2,1}$ is the ratio of isotopes *2* and *1* in the evaporating source. The ratio of the isotopic fluxes $J_{i,2}/J_{i,1}$ in the evaporating gas to the ratio $R_{2,1}$ defines the isotopic fractionation factor $\alpha_{2,1}$ ($\alpha_{2,1} = (\gamma_{i,2}/\gamma_{i,1})\sqrt{m_{i,1}/m_{i,2}}$). If the fractionation factor $\alpha_{2,1}$ remains the same as evaporation proceeds, the isotopic composition of the evaporation residues should evolve via Rayleigh fractionation given as:

$$R_{2,1} = R_0 f_i^{\alpha_{2,1}-1} \quad (6)$$

and

$$\ln(R_{2,1}/R_0) = (\alpha_{2,1}-1)\ln f_i \quad (7)$$

where $R_{2,1}$ is the ratio of isotopes *2* and *1* of a given chemical element *i* in the evaporation residue (^{25}Mg/^{24}Mg or ^{26}Mg/^{24}Mg for magnesium isotopes, and ^{29}Si/^{28}Si or ^{30}Si/^{28}Si for silicon isotopes), R_0 is their isotopic ratio in the starting material prior to evaporation, f_i is the fraction of the major isotope *1* (^{24}Mg or ^{28}Si) remaining in the residue after evaporation. Knowledge of precise values of $\alpha_{25,24}$ for fractionation of ^{25}Mg and ^{24}Mg and $\alpha_{29,28}$ for fractionation of ^{29}Si and ^{28}Si is required to reconstruct chemical composition of precursor material prior to evaporation using current bulk chemical and isotopic compositions of evaporation residues.

The relationships above can also be used to describe evaporation into low-pressure hydrogen gas provided that the effect of hydrogen on $P_{ij,sat}$ is taken into account.

3. EXPERIMENTAL TECHNIQUE AND ANALYTICAL METHODS

3.1 Starting materials and experimental protocols

A synthetic melt (labeled as CAI4B2) composed of 16 wt% MgO, 36% SiO_2, 27% Al_2O_3, and 21% CaO was used as a starting material for evaporation experiments. In a Fo-An-Geh ternary diagram the composition plots close to those of non-FUN forsterite-bearing (FoBs) CAIs studied by Bullock et al. (2012). These FoBs appear as fine-grained CAIs that have experienced only minor thermal processing which resulted in their sintering or small degree of melting to their outer parts. Another batch of this material (labeled as CAI4) was earlier evaporated at 1900ºC in vacuum (Mendybaev and Richter, 2016). These experiments showed that melting and evaporation of magnesium and silicon from the CAI4 melt results in compositions close to those of "normal" compact Type A and coarse-grained Type B CAIs.

The starting composition for the experiments was prepared first by mixing dried powders of MgO (Alfa Aesar, 99.998%), SiO_2 (Aldrich®, >99.995%), Al_2O_3 (Alfa Aesar®, 99.99%), and $CaCO_3$ (Alfa Aesar®, 99.99%) in agate mortars under ethanol for at least 60 min followed by its

further homogenization in a Retsch® MM200 oscillating mill using a 5 ml agate jar and two 7 mm agate balls under ethanol at 20 cycles per second for at least 400 min. After the mixture was dried at room temperature, it was placed into a platinum crucible that was heated at 1000°C for ~10 h to drive off CO_2 from the calcium carbonate. The fine mixture of oxides was then cooled under vacuum and stored for later use in a desiccator connected to a vacuum pump. Individual evaporation experiments were conducted on samples with 10–40 mg of the powder mixed with polyvinyl alcohol and loaded onto 1.5- and 2.5-mm diameter iridium wire loops (Alfa Aesar®, 99.8%) of a known weight. The Ir-wire loops with a sample were allowed to dry at 25°C overnight, weighed and then heated in a Deltech vertical furnace at 1000°C for ~5 min to drive off the polyvinyl alcohol and sinter the powder. The final step of the sample preparation was to melt the sample in a Deltech furnace at 1550ºC for 10 min in a flowing H_2-CO_2 gas mixture with oxygen fugacity (f_{O2}) corresponding to the QMF (quartz–magnetite–fayalite) buffer. This f_{O2} is sufficiently oxidizing that evaporation of Mg and Si from the melt is negligible, but sufficiently reducing not to oxidize and evaporate Ir from the iridium wire loop. The molten samples were quenched by pulling the Ir-wire loop with the sample from the furnace hot spot. The weight of the sample with Ir-wire loop was measured again to obtain the amount of material in the loop by subtracting the weight of Ir-wire loop from the total weight of the loop plus the molten droplet assemblage. The surface area of the samples was determined by measuring the diameter of the Ir-wire loop and the thickness of droplet at the center of the loop before and after evaporation experiments. The surface area of samples at 1600°C was calculated using the thermal expansion coefficient of Ir, and density-composition-temperature relationships of Lange and Carmichael (1987) for the melt. In the calculations we also considered that a part of the 0.25 mm thick Ir-wire loop was partially (or completely in case of large, >30 mg, samples) wetted by melt. This increases the effective loop diameter (from 2.5 mm to 2.75 mm or 3.0 mm, for example). The difference in the sample surface area calculated using the measured sample geometry and calculated ones agree with each other within 10%. The initial and the final surface areas of the samples in Table 1 are based on the calculated thicknesses of the samples.

Since some loss of Mg and Si from the sample might take place while the furnace temperature was ramped up from room temperature to the experimental temperature of 1600°C, the possible mass loss and chemical and isotopic fractionations during such a heating needs to be compensated for. This was done by using sample B2-1, which was heated in vacuum at 1600°C for 5 minutes and quenched (Table 1), as the effective chemical and isotopic composition of the starting material. The sample underwent the least evaporative loss (only ~0.2 mol% of Mg and Si, Table 1) and thus was considered as the "zero-time residue". Because low-P_{H_2} experiments the furnace was also first heated to 1600°C in vacuum and kept at this temperature for 5 minutes before H_2 was introduced (see Section 3.1.2 for the experimental details), composition of B2-1 was used as the effective starting composition in these experiments also. The fractions of Mg and Si evaporated and the associated isotopic compositions in all evaporation residues presented in Table 2 were calculated relative to that of sample B2-1.

3.1.1 Vacuum evaporation experiments

The vacuum evaporation experiments were performed in a high-temperature, high-vacuum furnace at the University of Chicago (Hashimoto, 1990) with a tungsten mesh heater (45 mm in diameter and 150 mm in height) surrounded by several layers of a molybdenum/tungsten

heat shield. Temperature was measured using two factory calibrated Type G (W-W26Re) thermocouples located within ~10 mm on both sides of the sample and with a PYRO Micro-optical pyrometer at ~5 mm below the sample. The temperatures measured by two thermocouples and pyrometer at 1400˚C to 2000˚C agreed to within ±5˚C.

After a sample loaded onto an Ir-wire loop was placed into the furnace at room temperature, the furnace was pumped down to about 10^{-7} bars, and the temperature was then raised in a manual mode to 900ºC in about an hour followed by heating at 20ºC/min to 1400ºC. This temperature was held at 1400°C for 30 min to ensure complete degassing of the sample as indicated by pressure drop back to ~10^{-7} bars. The temperature was then raised to the final run temperature of 1600ºC at 40ºC per minute and each sample was allowed to evaporate for a predetermined amount of time. The furnace temperature during the run was maintained by a Eurotherm temperature controller to within ±1°C, and the experiment was ended by cutting the power to the heater. The furnace cooled to 500ºC within a minute and to room temperature in two hours. The turbomolecular pump was then turned off, the furnace was vented, and the sample was removed from the furnace. After the final weight (Ir-wire loop plus quenched melt) and thickness of the evaporation residue were measured, the sample was broken into several pieces for separate chemical and isotopic analysis. The experimental procedure was the same in all runs (including B2-1), with the run duration being the only variable.

3.1.2 Low-pressure H_2 experiments

Several sets of samples prepared at the University of Chicago were run in the low-pressure high-temperature hydrogen furnace at Hokkaido University. The experiments were conducted at the 1600°C with P_{H_2} ~2×10^{-4} and ~2×10^{-5} bars in a continuously evacuated stainless-steel vacuum furnace with a tungsten mesh heater (25 mm in diameter and 100 mm in height) surrounded by several layers of a molybdenum heat shield (Takigawa et al., 2009). The sample temperature was monitored with a molybdenum-sheathed Type C thermocouple (W5Re–W26Re) placed 22.5 mm above the sample location. The thermocouple was calibrated against the melting temperatures of metallic iron (1535°C), nickel (1455°C) and the eutectics of Rh–C (1657°C) by placing the metals and alloys in the same location where samples were later positioned. Pressure inside the furnace was measured by both a Pirani and an ionization gauge. After the chamber with a sample was evacuated at room temperature to 10^{-9}–10^{-10} bar by a turbo pump, the furnace was preheated to 500°C, and held at that temperature for 0.5–1 hour. When the chamber pressure dropped below 5×10^{-9} bar, the sample was further heated to the experimental temperature of 1600°C at the rate of ~20°C per minute and held at this temperature for 5 min to ensure complete melting of the sample, and then H_2 gas was introduced into the chamber (between the heater and the heat shield) at a flow rate to maintain constant pressure (~2×10^{-4} or ~2×10^{-5} bar) during the experiment. Samples were heated for the desired duration (Table 1) and then cooled by turning off the heater (the temperature dropped to 1000°C with a couple of minutes and to 500ºC in ~20 minutes). After the temperature dropped to 25°C, the sample was removed from the furnace, weighed and the sample geometry was measured. The weight change and surface area were used to determine the bulk evaporation kinetics. Evaporative fluxes of Mg and Si in all experiments were calculated using the chemical composition of the residues relative to B2-1 that was evaporated at 1600°C for 5 minutes in vacuum (see above).

3.2 Analytical techniques

The experimental run products were cut into several pieces: one was mounted in epoxy and polished to study texture and chemical composition, and two smaller chips were used for Mg and Si isotopic studies.

3.2.1 Chemical composition of evaporation residues

The texture and chemical composition of the CAI4B2 evaporation residues were studied using the TESCAN LYRA3 FIB/FESEM (Focused Ion Beam / Field Emission Scanning Electron Microscope) at the University of Chicago equipped with Oxford Instruments AZtec Energy Dispersive Spectrometer (EDS) microanalysis system with two 80 mm^2 XMax silicon drift EDS detectors. Backscattered electron (BSE) and secondary electron (SE) images were used to characterize the evaporation residues. The chemical composition of the samples was determined either by averaging at least 20 spots analyzed across the sample (for the residues quenched as glass) or by averaging the results of scanning 15–20 areas of ~250×200 μm in size for the residues that appear as an intergrowth of different minerals and glass. The working conditions involved a 15 kV accelerating voltage and ~5 nA beam current; natural and synthetic materials were used as calibration standards. The chemical compositions of the evaporation residues are presented in Table 1. The chemical composition of the samples along with their surface area (average of the initial and final) and run durations was used to calculate the evaporation rates J_{Si} and J_{Mg}. Since aluminum is very refractory element and does not evaporate under the conditions of the experiments, the fractions of Mg and Si lost during evaporation (Table 2) were calculated as the ratio of oxide/Al_2O_3 in residues normalized to their ratio in B2-1.

3.2.2 Magnesium isotopic analyses

Magnesium isotopic compositions of the experimental run products were measured at the Department of Earth and Space Sciences of the University of Washington, Seattle, following the method described in detail by Teng and Yang (2014) and Teng et al. (2010, 2015a, 2015b). About 1 to 3 mg of evaporation residues (~50 to 250 μg of Mg) were dissolved sequentially in Optima-grade concentrated HF–HNO_3, HNO_3–HCl, and HNO_3. The final solutions were made by taking up the samples in 1N HNO_3. One hundred microliters of the final solution then was loaded onto precleaned Bio-Rad cation-exchange resin (AG50W-X8, 200–400 mesh) for purification and separation of Mg. The purification procedure was repeated several times to ensure maximum elimination of matrix effects due to presence of elements other than magnesium.

Magnesium isotopic composition of the samples was measured on a *Nu Plasma* II Multi-Collector Inductively Coupled Plasma Mass Spectrometer (MC-ICP-MS). Sample solutions were introduced into the ion source with "wet" plasma condition. To minimize the effect of evaporation during a batch run all sample and standard DSM-3 solutions were prepared at the day of measurement using the same batch of 3% Optima-grade HNO_3. At a typical Mg concentration of 300 ppb, ^{24}Mg background is negligible ($<10^{-4}$ V) compared to sample signals (3–4 V). The instrumental fractionation was corrected by sample-standard bracketing technique

assuming a linear mass fractionation drift during a batch run. All Mg isotope data are reported in delta (δ) notation defined as

$$\delta^{x}Mg = 1000 \times \left(\frac{(^{x}Mg/^{24}Mg)_{sample}}{(^{x}Mg/^{24}Mg)_{standard}} - 1 \right)$$

The δ^{25}Mg and δ^{26}Mg values reported are in parts per thousand (‰) deviations of a ratio relative to the average of the two standard ratios measured before and after.

The accuracy of the measurements was assessed by measuring the Mg isotopic composition of BHVO-2 and seawater used as standards which were processed the same way as all CAI4B2 samples. The isotopic composition of the standards measured in this study relative to DSM-3 (δ^{25}Mg = –0.44±0.05 and δ^{26}Mg = –0.82±0.05 for seawater and δ^{25}Mg = –0.11±0.05 and δ^{26}Mg = –0.25±0.06 for BHVO-2; uncertainties are 2SD) are identical within error as those reported in the literature (e.g., Teng et al., 2015a, 2015b) which ensures accuracy of the Mg isotopic composition measurements reported here.

3.2.3 Silicon isotopic analyses

The silicon isotopic compositions of experimental run products were measured at the University of St Andrews (UK) and the Water Quality Centre of Trent University (Canada). Prior to Si isotope analysis, all the experimental charges, external standards and bracketing standard were processed identically via an alkali-fusion and ion chromatography technique, as described by Georg et al. (2006) with modifications described in Savage and Moynier (2013).

To transfer each experimental charge into solution, the run products were attacked via an HF-free alkali fusion technique. The use of HF acid is avoided, as HF reacts with Si to form the volatile compound SiF_4, which could result in loss (and consequent isotope fractionation) of a sample's Si. Briefly, each experimental run product (0.25–9 mg) was weighed into a precleaned silver crucible, composed of 99.9% purity Ag. About 100–150 mg of NaOH flux (Sigma-Aldrich, semiconductor grade, >99.99% pure) was then added in pellet form to each of the crucibles. The crucibles were then placed in a preheated muffle furnace, at 720°C, for at least 15 minutes. After removal from the furnace, each crucible, containing a fusion cake, was submerged into 20 ml of ultrapure deionized water (MQ-e Millipore Water, 18.2 MΩ·cm) in a precleaned PTFE vial, sealed and left overnight.

Each fusion cake was removed from its crucible via ultrasonication, and the subsequent solution transferred via pipette into a precleaned polypropylene (PP) bottle (Nalgene) – the crucible was rinsed with MQ-e water, which was again transferred into the same PP bottle. Finally, the sample solution was acidified with thermally distilled concentrated HNO_3, to a final molarity of ~0.16 M – the volume of concentrated HNO_3 used in this step is calculated based on the mass of NaOH used in the alkali fusion, and the volume of solution in each PP bottle.

The Si concentration of each sample solution was measured using a Thermo Scientific Evolution 200 UV-VIS spectrophotometer utilizing the "heteropoly blue" method (Hach-Lange ultra-low range silica reagent kit) – this acts as a check of fusion yield (all between 95% and 99% total Si recovery in this study) as well as to establish how much sample solution was required for isotope purification.

All standards and samples were purified prior to Si isotope analysis via a single-stage ion chromatography technique. A detailed description of this method can be found in Georg et al. (2006), and the specific reagent types, strengths and quantities for each step are provided in Savage and Moynier (2013). In short, each sample was loaded onto 1.8 ml of precleaned BioRad AG50W-X12 cation exchange resin (200–400 mesh) and eluted through the column using 5 ml of MQ-e water. This quantitatively separates Si from all major cationic species in the solution, because at low pH, Si is in solution as either a neutral or anionic species. All other anions or neutral species in the sample solutions are at too low relative concentrations to affect isotope measurement.

Most of the silicon isotope measurements were performed on the *Neptune Plus* (Thermo-Finnigan, Bremen) MC-ICP-MS instrument in the St Andrews Isotope Geochemistry (STAiG) laboratories at the University of St Andrews. Samples were introduced to the instrument via a 75 µl min^{-1} ESI Microflow self-aspirating nebulizer running into a Thermo Scientific SIS cyclonic glass spray chamber. The instrument was operated at "medium" resolution ($M/\Delta M \approx 6500$) to allow for the interference-free analysis of all three Si isotope beams.

Samples were analyzed at concentrations of 1.0 or 0.5 ppm Si, which resulted in signals of ~10 V or ~5 V respectively on the ^{28}Si beam, using standard 10^{11} Ω resistors. The choice of concentration was made based on the amount of Si available in each sample aliquot – the lower concentration samples were analyzed at 0.5 ppm Si. Silicon blanks monitored during analysis were measured as ≈ 0.04 V on the ^{28}Si beam, which equates to approximately 4 ppb Si, and is therefore negligible (<1%) compared to sample concentrations. Nevertheless, online blank corrections were performed on each measurement.

Silicon isotope ratios were measured in static mode and a measurement consisted of 22 cycles of 3 s integrations with a 3 s idle time. Isotope measurements were calculated using the standard-sample bracketing method, with NBS 28 (NIST RM 8546) as the bracketing standard, in permil (‰) as follows:

$$\delta^{x}Si = 1000 \times \left(\frac{(^{x}Si/^{28}Si)_{sample}}{(^{x}Si/^{28}Si)_{standard}} - 1 \right)$$

where x = 30 or 29, depending on the ratio. During each analysis session, aliquots of the USGS geostandards BHVO-2 ($\delta^{30}Si$ = −0.30±0.03‰ @ 1ppm; $\delta^{30}Si$ = −0.28±0.10‰ @ 0.5ppm) and BCR-2 ($\delta^{30}Si$ = −0.26±0.04‰ @ 0.5 ppm Si), and established Si isotope standard Diatomite ($\delta^{30}Si$ = 1.19±0.05‰ @ 1 ppm Si) were run to assess external accuracy. These agree well with previously published values (Reynolds et al., 2007; Savage et al., 2014) and with those same standards (different aliquots) analyzed at Trent University (see later). Analytical precision is represented as the 2 standard deviation (2SD) calculated on the 4 or 5 delta values generated from repeated analyses of each sample during the same analytical session. Typical analytical precision for the samples analyzed at 1 ppm ranges between $\delta^{30}Si$ ±0.03 and ±0.10 ‰ (2SD), which is comparable to recent measurements made in the same laboratory and elsewhere (e.g., Savage et al., 2014; Trail et al., 2018). For those samples analyzed at 0.5 ppm, (i.e. where we were sample-limited) analytical precision is generally twice as poor, most likely as a result of lower signal-to-noise ratios on the ^{30}Si and ^{29}Si (minor) isotope beams.

Silicon isotopic composition of a set of samples was also obtained using *Nu Plasma 1700* High Resolution MC-ICP-MS at the Water Quality Centre of Trent University (Peterborough,

Ontario, Canada) using the same procedure described above. The accuracy and reproducibility of the measurements were assessed using Diatomite (δ^{30}Si = +1.25±0.09‰, 2SD), Quartz Merck (δ^{30}Si =−0.05±0.06‰) and BHVO-2 (δ^{30}Si = −0.26±0.09‰) as reference materials, which agree well with the established values, as well as those from the University of St Andrews (see above).

4. EVAPORATION KINETICS AND ELEMENTAL FRACTIONATION

The experimental conditions, chemical compositions of evaporation residues and the calculated evaporation rates of Mg and Si from a CAI-like melt are presented in Table 1, and Mg and Si isotopic compositions of the samples are presented in Table 2. The data are used to test how evaporation of a CAI-like melt in vacuum and in low-pressure hydrogen-rich conditions affects chemical and isotopic evaporation trends, and thus if the extensive existing experimental datasets on vacuum evaporation of different composition CAI-like melts can be used to model evaporation of early solar system materials in more realistic solar nebula conditions. Finally, we use the experimental results to estimate durations of heating events required to produce the chemical and isotopic signatures typical for "normal" Type A and B CAIs and highly fractionated Type F and FUN CAIs by evaporation of their precursor materials in solar nebula gas.

4.1. Evaporation kinetics in vacuum and low-P_{H_2} experiments

The typical textures of run products from the FoB-like CAI evaporation experiments are shown in Fig. 1. The least evaporated residues with bulk chemical composition within the melilite stability field appear as clear glasses as shown in Figure 1a for sample B2-16 that was evaporated for 10 minutes at 1600°C and P_{H_2}~2×10^{-4} bar. Such samples are chemically homogeneous without any concentration gradients between the central and outer parts of the samples. This suggests that Mg and Si diffusion in the melt at 1600°C is faster compared to the loss of Mg and Si due to evaporation from the near-surface areas of molten droplets. The residues with the highest degree of evaporation that lost most of their Mg and Si are comprised of intergrowths of Ca-aluminates ($CaAl_2O_4$) and glass (Fig. 1c). The residue B2-10 that was evaporated for 45 minutes at P_{H_2}~2×10^{-4} bar was the only sample that appeared as an intergrowth of relatively large elongated gehlenitic melilite and glass (Fig. 1b). The texture suggests that melilite crystallized from the melt rather than during quench, which in turn would require the experimental temperature to be below the liquidus temperature of 1590°C for the åkermanite-gehlenite binary (Osborn and Schairer, 1941; Mendybaev et al., 2006b). Below we will demonstrate that Mg and Si isotopic compositions of the samples containing significant amount of Ca-aluminates (B2-4, B2-18, B2-19, B2-20, B2-30, B2-32) and sample B2-10 containing only traces of $CaAl_2O_4$ plot off the trend typical for glassy samples with compositions within the melilite stability field. Only samples with bulk chemical compositions in the melilite field were used to determine isotopic fractionation factors.

Evaporation kinetics from low-pressure experiments expressed as a total weight loss of the CAI4B2 samples per unit surface area (average of the initial and final) are presented in Table 1. Figure 2 shows that the surface area normalized bulk weight loss is a linear function of time, and that P_{H_2} strongly increases the total evaporation rates from $(2.4\pm0.1)\times10^{-5}$ g cm^{-2} min^{-1} in vacuum experiments to $(4.5\pm0.2)\times10^{-4}$ g cm^{-2} min^{-1} at 2×10^{-5} bar H_2 and $(1.1\pm0.1)\times10^{-3}$ g cm^{-2}

409 min^{-1} at 2×10^{-4} bar H_2. The important observation is that the relative evaporation rates of Mg
410 and Si, obtained using the chemical composition of the CAI4B2 evaporation residues (Table 1),
411 are independent of P_{H_2} with the average evaporation rates $J_{Mg}=(3.6\pm0.4)\times10^{-9}$ and
412 $J_{Si}=(4.0\pm0.5)\times10^{-9}$ mol cm^{-2} s^{-1} in vacuum, $J_{Mg}=(5.6\pm0.3)\times10^{-8}$ and $J_{Si}=(6.7\pm0.9)\times10^{-8}$ mol cm^{-2}
413 s^{-1} at 2×10^{-5} bar H_2, and $J_{Mg}=(1.6\pm0.4)\times10^{-7}$ and $J_{Si}=(1.9\pm0.5)\times10^{-7}$ mol cm^{-2} s^{-1} at 2×10^{-4} bar
414 H_2 with relative evaporation rates J_{Mg}/J_{Si}~1 in all experiments. The results show that evaporation
415 rates of Mg and Si from CAI4B2 melt at 2×10^{-4} bar H_2 are ~2.8 times faster than at 2×10^{-5} bar
416 H_2 and ~45 times faster than in vacuum, and that the rates at 2×10^{-5} bar H_2 are ~19 times faster
417 than in vacuum. Faster evaporation of Mg and Si in H_2-rich gas and independence of J_{Mg}/J_{Si} on
418 imposed P_{H_2} are in agreement with thermodynamic expectations (e.g., Tsuchiyama et al., 1999;
419 Grossman et al., 2000) that saturation vapor pressures of $Mg_{(g)}$ and $SiO_{(g)}$ should be independent
420 of P_{H_2} of the surrounding gas at low P_{H_2} (<10^{-7} bar in the case of CMAS melt evaporated at
421 1727°C, Grossman et al., 2000), but increases as a function of $\sqrt{P_{H2}}$ with increase of P_{H_2} at
422 higher pressures. These relationships will be discussed in more detail in Section 6.

423 The evaporation rate of silicon for CAI4B2 melt in vacuum experiments at 1600°C is the
424 same as $(3–4)\times10^{-9}$ mol cm^{-2} s^{-1} determined by Richter et al. (2007) for their Type B CAI-like
425 melt that was evaporated under the same conditions, while our J_{Mg} is about twice as large. This is
426 illustrated in the Arrhenius plot (Fig. 3) that shows the temperature effect on evaporation kinetics
427 for different composition melts evaporated in vacuum and at low-P_{H_2}. We should note that B133
428 and B113 melts (Richter et al., 2002) and Type B CAI-like (we will refer to latter as CAIB) melt
429 (Richter et al., 2007) are very close chemically and contain ~12–13 wt% MgO and ~46–48 wt%
430 SiO_2. This explains why J_{Mg} and J_{Si} for these compositions plot along the same regression line
431 through all available data with the activation energies $E_{a,Si}$ = 564±42 kJ mol^{-1} for silicon and
432 $E_{a,Mg}$ = 553±32 kJ mol^{-1} for magnesium evaporation, which are the same as reported by Richter
433 et al. (2007). The dashed lines in Fig. 3 passing through the CAI4B2 and BCAI (Richter et al.,
434 2002) data from 2×10^{-4} bar H_2 experiments are the ones obtained using E_a from the vacuum
435 experiments above. It should be noted here that CAI4B2 and BCAI melts are chemically close:
436 CAI4B2 melt contains ~16 wt% MgO and 36 wt% SiO_2 with CaO/Al_2O_3 ~ 0.8, while BCAI melt
437 contains ~18 wt% MgO and 37 wt% SiO_2 with CaO/Al_2O_3 ~ 1.2. The fact that activation
438 energies appear to be the same for vacuum and low-P_{H_2} evaporation suggests that the rate-
439 limiting step of the evaporation is the same despite very large differences in evaporation kinetics.
440 The reason why J_{Si} ~ J_{Mg} in CAI4B2 experiments and J_{Mg} ~2 J_{Si} for CAIB melts most likely is
441 related to activities of MgO and SiO_2 and evaporation coefficients of $Mg_{(g)}$ and $SiO_{(g)}$ in the
442 melts. We will address this in Section 6.

443

444 ***4.2. Elemental fractionation in vacuum and low-P_{H_2} experiments***

445 Since only Mg and Si evaporate under the conditions of these experiments (Al remains in
446 the melt and Ca evaporates only when Mg and Si are nearly completely lost), evolution of melt
447 composition can be expressed as the percentage of Mg and Si lost or wt% MgO/Al_2O_3 versus
448 wt% SiO_2/Al_2O_3 ratios in the residual melts. These relationships are shown in Figure 4 for
449 CAI4B2 melt (top panels) and, for reference, CAIB melt (bottom panels). The main feature of
450 the figure is that all evaporation residues from CAI4B2 experiments at 1600°C plot along a

single curve regardless of experimental conditions (vacuum or low-P_{H_2}) and sample size (1.5 and 2.5 mm) used in the experiments. During evaporation the percent of Mg and Si lost linearly correlate with each other (Mg:Si ~ 3:2) and remain the same until nearly all Mg is evaporated. The residues from 1900°C vacuum experiments are slightly displaced relative to those from 1600°C runs toward more Mg-rich and/or Si-poor compositions (CAI4 and CAI4B2 are two batches of the same material). This is due to somewhat faster loss of silicon over magnesium in 1900°C runs at the initial stages of evaporation followed by the loss of Mg and Si at the same 3:2 proportions as in 1600°C runs. Presence of $CaAl_2O_4$ in the most evaporated residues from 1600°C and lack of such in residues from 1900°C runs is due to the relatively low crystallization temperature of $CaAl_2O_4$ (T_{cryst} ~1500°C in CaO-Al_2O_3 system with wt% CaO/Al_2O_3 ~0.8 which increases to 1605°C for melts with CaO/Al_2O_3 ~0.5; Ustunisik et al. (2014) found T_{cryst}=1487C, for glass + grossite from a CMAS melt representing predicted CAI-like condensates). Evaporation of even more Ca-depleted melts (like CAI 5aN-like with CaO/Al_2O_3 ~0.3, Ivanova et al., 2018) at 1900°C results in evaporation toward Ca-aluminates with hibonite ($CaAl_{12}O_{19}$, T_{cryst}=1833°C), grossite ($CaAl_4O_7$, T_{cryst}=1765°C) and $CaAl_2O_4$ as the quench products in the most evaporated residues.

Panels *c* and *d* in Fig. 4 show the same relationships as panels *a* and *b* but for Type B CAI-like CAIB molten droplets of 1, 2.5 and 6 mm in size evaporated at 1600°, 1700°, 1800° and 1900°C in vacuum (Richter et al., 2007). The starting CAIB melt is enriched in silicon (SiO_2/Al_2O_3 =2.4) compared to the CAI4B2 melt (SiO_2/Al_2O_3 =1.3), and as such its evaporation starts with much faster loss of Si over Mg. However, after ~20% Mg and ~40% Si are evaporated, Mg evaporates ~2.5 times faster than Si until almost all Mg is lost. The most important features in Fig. 4c and 4d are that there are no obvious temperature and sample size effects on evaporation trajectories causing all trajectories essentially to plot on top of each other.

Experimentally determined evaporation rates of silicon and magnesium from low-pressure H_2 experiments (Table 1 and Fig. 3) indicate that at 1600°C in solar nebula environments it would take ~20 minutes at P_{H_2}~2×10^{-4} bar and less than an hour at P_{H_2}~2×10^{-5} bar to evaporate ~30% Mg and ~25% Si from a 2.5 mm CAI-like droplet. The timescales required to produce depletions of magnesium and silicon and to fractionate their isotopes to the levels observed in CAIs by evaporation of a CAI precursor in solar nebula gas will be discussed in Section 7.

5. ISOTOPIC FRACTIONATION

Evaporation of melts under low-pressure conditions results in loss of moderately volatile Mg and Si and associated chemical and isotopic fractionations. The isotopic fractionation is due to faster evaporation of lighter isotopes of an element that result in enrichments of evaporation residues in the heavier isotopes. Magnesium and silicon isotopic compositions of CAI4B2 evaporation residues from vacuum and low-P_{H_2} experiments are presented in Table 2 and in Figure 5. Table 2 shows the measured $\delta^{25,26}$Mg and $\delta^{29,30}$Si values and those normalized to the least evaporated sample CAI4B2-1 (Table 1). As stated earlier, the purpose of such normalization is to eliminate the possible chemical and isotopic fractionations of Si and Mg while the furnace ramps up to the experimental temperature.

Figure 5 shows a smooth correlation between δ^{25}Mg and δ^{29}Si in the CAI4B2 residues from both vacuum and 2×10^{-4} bar H_2 experiment except for sample B2-10 (circled in Fig. 5). This sample is the only one of all evaporation residues that contains a large amount of melilite (Fig. 1b) with textures suggesting that it crystallized from the melt during the run and is not a quench product. As it was noted above all other CAI4B2 residues with bulk composition within the melilite stability field appear as a clear glass. The reason why melilite have crystallized in B2-10 run, but not in other experiments, is most likely due to the actual run temperature in the run being lower than the targeted 1600°C. Melilite crystallizing from the melt should be isotopically lighter than the coexisting melt that continued to evaporate and further fractionate Mg and Si isotopes after melilite crystallization. The presence of isotopically lighter melilite in the final run product could explain why the bulk Mg and Si isotopic compositions of B2-10 plot off the correlation line based on melilite-free samples shown as solid curve in Fig. 5.

Labeled in Fig. 5 are samples from the 2×10^{-4} bar H_2 experiments using CAI4B2 melt; also shown are run durations. Sample B2-3 is the most isotopically fractionated one, although it was evaporated for 30 minutes, compared to less fractionated B2-14 that was evaporated for 35 minutes. The reason for this is that B2-3 is about half as large as B2-10, B2-12 and B2-14 shown in Fig. 5 (Table 1). The faster evaporation of sample B2-3 is at least in part the result of the smaller sample having a greater surface area to volume ratio. The facts that B2-3 contains some minor amounts of $CaAl_2O_4$ and its bulk composition plots outside of the melilite stability field, provides further support that this sample has lost more Mg and Si compared to all other residues in Fig. 5. All evaporation residues in Fig. 5, except for B2-3 and B2-10, appear as clean glasses with bulk compositions within the melilite stability field.

Figure 5 also shows magnesium and silicon isotopic compositions of CAIB evaporation residues (open symbols) evaporated at 1600° to 1900°C (Richter et al., 2007; Knight et al., 2009). In accord with Fig. 4, evaporation of the CAIB melt starts with much faster loss of Si compared to Mg that results in the CAIB residues being significantly enriched in heavy δ^{29}Si compared to the CAI4B2 residues. After the initial stages (when δ^{25}Mg > 6 in Fig. 5), the change in δ^{29}Si versus δ^{25}Mg in CAIB residues becomes close to that in CAI4B2 residues. An important feature of Fig. 5 is that magnesium and silicon isotopic compositions of the CAIB residues produced in 1600°C, 1800°C and 1900°C experiments plot along a single correlation curve (dashed) suggesting very weak, if any, temperature effect on the isotopic fractionation within the range of δ^{25}Mg and δ^{29}Si shown in the plot. When CAIB residues with δ^{25}Mg>25‰ were taken into account, significant temperature effect on Mg isotopic fractionation was found (Richter et al., 2007); no such temperature effect was observed for Si isotopic fractionation in the same CAIB residues (Knight et al., 2009).

Figure 5 shows that the heavy isotope enrichments of δ^{25}Mg ~5–10‰ and δ^{29}Si ~2–4‰ typical for coarse-grained Type A and B CAIs (e.g., Grossman et al., 2000; 2008) can be produced within ~30 minutes of evaporation of a ~2.5 mm diameter FoB CAI-like precursor at 1600°C in the solar nebula with $P_{H_2}\sim2\times10^{-4}$ bar. The effect of pressure and temperature on timescales required to produce the chemical and isotopic signatures of natural CAIs will be discussed in more details in the Section 7.

5.1 Magnesium isotopic fractionation

The Mg isotopic composition of evaporation residues is presented in Table 2 and Fig. 6. Also plotted in Fig. 6 are the Mg isotope data from the evaporation experiments of Richter et al. (2002, 2007). The most important finding from the experiments is that all experimental data from both vacuum and low-pressure H_2 experiments, using different composition melts evaporated at both 1600°C and 1500°C, plot along the same regression line, defining the same Mg isotopic fractionation factor.

Magnesium isotopic composition in Fig. 6 is expressed as $\ln(R/R_0)$, where R is $^{25}Mg/^{24}Mg$ in the sample and R_0 is the ratio in the starting material, as a function of Mg remaining in residues expressed as $\ln f_{24Mg}$. Shown are the results from vacuum (closed circles) and 2×10^{-4} bar H_2 (diamonds) experiments using 2.5-mm diameter CAI4B2 samples, as well as the results of Richter et al. (2007) for Type B CAI-like (CAIB) melt evaporated in vacuum at 1600°C (open circles) and that of Richter et al. (2002) for BCAI melt evaporated at 2×10^{-4} bar H_2 at 1500°C (half-filled squares). The figure shows that Mg isotopic composition linearly correlates with $\ln f_{24Mg}$ confirming that evaporation is a Rayleigh distillation process (Eqs. 6 and 7) with the slope of the line corresponding to $\alpha_{25,24} - 1$. Figure 6 shows that experimental data from the CAI4B2, CAIB and BCAI experiments plot along the same regression line with the slope corresponding to $\alpha_{25,24} = 0.9877 \pm 0.0004$ ($\alpha_{25,24}$ is 0.98786 ± 0.00032 for vacuum and 0.98745 ± 0.00026 at 2×10^{-4} bar H_2 experiments using CAI4B2 melt; $\alpha_{25,24} = 0.98759 \pm 0.00041$ for BCAI melt evaporated at 1500°C and 2×10^{-4} bar H_2; $\alpha_{25,24} = 0.98822 \pm 0.00010$ for CAIB melt evaporated at 1600°C in vacuum). To account for a loss of magnesium and silicon and their possible isotopic fractionations during furnace heat up to the experimental temperature, Mg isotopic composition and fraction of Mg lost in all evaporation residues here have been recalculated by normalizing to the least evaporated sample in each experimental set at a given temperature. Sample B2-3 (circled in Fig. 6) was not included in the regression for CAI4B2 residues as its bulk composition plots outside of the melilite stability field. The linear dependency of Mg isotopic composition on the amount of Mg remaining in the melt in Fig. 6 also suggests that there is no recondensation of Mg back into the melt that would result in lower than expected $\delta^{25}Mg$ in highly evaporated samples. The lack of Mg recondensation was previously demonstrated by Richter et al. (2007) in their vacuum experiments using samples of very different sizes (1 to 6 mm in diameter).

The fact that the Mg isotopic composition of sample B2-3, containing some $CaAl_2O_4$, plots away from the regression line in Fig. 6 (with $\alpha_{25,24} = 0.9877\pm0.0004$ obtained for melilitic residues), might indicate a dependence of $\alpha_{25,24}$ on melt structure. This is in agreement with results of Mendybaev et al. (2013a, 2017) who showed that $\alpha_{25,24}$ for forsteritic and melilitic melts are significantly different with $\alpha_{25,24} = 0.98372\pm0.00041$ for forsteritic and $\alpha_{25,24} = 0.98567\pm0.00046$ for melilitic melts evaporated at 1900°C in vacuum. We might expect that the $\alpha_{25,24}$ value would further increase as the melt composition evolves from melilitic toward $CaAl_2O_4$-rich melts.

Richter et al. (2007) found that $\alpha_{25,24}$ for melilitic melt slightly decreases with temperature from 0.98822 ± 0.00010 at 1600°C to 0.98607 ± 0.00017 at 1900°C. However, $\alpha_{25,24}$ appears to be the same in low-pressure H_2 experiments at 1600°C and 1500°C (Fig. 6). The temperature and composition effects on $\alpha_{25,24}$ in vacuum and low-P_{H_2} experiments are summarized in Fig. 7, which clearly illustrates the difference in $\alpha_{25,24}$ for melilitic and forsteritic melts. This fact needs to be considered while calculating the fraction of Mg lost due to

evaporation based on isotopic compositions of a CAI when reconstructing its precursor composition. The figure also shows that all experimentally determined $\alpha_{25,24}$ values are significantly different from the "ideal" $\alpha_{25.24} = \sqrt{24/25} = 0.97980$ calculated assuming that complete chemical equilibrium is reached in the gas phase such that magnesium evaporates as $Mg_{(g)}$. This discrepancy between calculated and measured fractionation factor has been shown in many experiments (e.g., Richter et al., 2002, 2007; Mendybaev et al. 2013a, 2017) and thus is clearly not an experimental artifact. The smaller experimental $\alpha_{25,24}$ could be explained if some magnesium escapes the melt as $MgO_{(g)}$ ($\alpha_{25.24} = \sqrt{40/41} = 0.98773$) or even more complex molecules, such as those determined in the gas phase above CMAS melts in Knudsen cell effusion experiments (e.g., Shornikov and Yakovlev, 2015).

5.2 Silicon isotopic fractionation

The most important finding from the experiments reported here is that Si isotopic fractionation factor remains the same regardless whether the melt evaporates in vacuum or in low-P_{H_2} solar nebula gas.

Figure 8 shows the silicon isotopic composition of CAI4B2 evaporation residues (closed symbols) expressed the same way as for magnesium isotopes in Fig. 6. Also plotted in Fig. 8 are the silicon isotopic composition from vacuum experiments (open symbols) for melilitic CAIB melt evaporated at 1600° to 1900°C (Knight et al., 2009) and for forsteritic FUN2 melt evaporated at 1700°C and 1900°C (Mendybaev et al., 2013a,b). The figure shows that similar to Mg isotopes, the Si isotopic composition of CAI4B2 residues plot along a single correlation line with slope corresponding to $\alpha_{29,28}$= 0.9910±0.0005 without any obvious differences between vacuum and low-P_{H_2} experiments, and between the droplets of different size. As is the case for Mg isotopes, sample B2-3 (circled diamond) was not included in obtaining the regression line for CAI4B2 residues (dashed line). Sample B2-30, which lost all its Mg and 97% of Si (–ln f_{28Si} = 3.64) and characterized by δ^{29}Si=15.04±0.20 (Table 2) was also rejected as its bulk chemical composition plots outside of stability field of melilite. Fig. 8 also clearly illustrate that unlike Mg isotopic fractionation factor, where different values for $\alpha_{25,24}$ were obtained for melilitic and forsteritic melts evaporated in vacuum, the value $\alpha_{29,28}$= 0.9901±0.0005 appears to be the same for both forsteritic (FUN2) and melilitic (CAIB) melts regardless of the experimental temperature. The somewhat lower Si isotopic fractionation obtained in experiments with molten Mg_2SiO_4 ($\alpha_{29,28}$= 0.9925±0.0001 at 1900°C; Davis et al., 1990) is likely due to Si recondensation caused by overly large initial sample masses (~200 mg) having been used in these experiments – we have avoided this by utilizing samples with initial mass less than 40 mg, close to natural CAIs in the most studied CV chondrites.

Similar to $\alpha_{25,24}$, the experimentally determined $\alpha_{29,28}$ is larger than $\alpha_{29.28} = \sqrt{(28+16)/(29+16)} = 0.98883$ expected if complete chemical equilibrium is reached in the gas phase and silicon evaporates as $SiO_{(g)}$. The calculated $\alpha_{29,28}$ would increase if some silicon escapes the melt as $SiO_{2(g)}$ ($\alpha_{29.28} = \sqrt{60/61} = 0.9918$) or more complex molecules, such as those determined in the gas phase above CMAS melts (e.g., Shornikov and Yakovlev, 2015).

6. THERMODYNAMIC MODELING OF EVAPORATION OF CMAS MELTS

Equilibrium thermodynamic calculations (e.g., Grossman et al., 2000; Ebel and Grossman, 2000)) and vapor speciation determined by Knudsen effusion mass spectrometry (e.g., Shornikov and Yakovlev, 2015; Costa et al., 2017) indicate that $Mg_{(g)}$ and $SiO_{(g)}$ are the most abundant Mg and Si gaseous species (>99%) in equilibrium with silicate melts and in an equilibrium vapor of solar or dust-enriched composition. Thus, evaporation of magnesium and silicon from completely molten CMAS melt into a vacuum is expected to occur mostly via the reactions:

$$MgO_{(melt)} \rightarrow Mg_{(g)} + 0.5O_{2(g)} \quad (8)$$

$$SiO_{2(melt)} \rightarrow SiO_{(g)} + 0.5O_{2(g)}. \quad (9)$$

In the case of free evaporation in vacuum, when gas released from the melt immediately leaves the gas/liquid interface without interacting with the melt, evaporation kinetics of the CMAS melt depends only on melt composition (i.e., activities of MgO and SiO_2 in the melt) and temperature. In this case the relative evaporation rates of Mg and Si can be expressed as:

$$\frac{J_{Si}}{J_{Mg}} = \frac{J_{SiO}}{J_{Mg}} \propto \frac{\gamma_{SiO}}{\gamma_{Mg}} \frac{a_{SiO2}}{a_{MgO}}. \quad (10)$$

where a_{MgO} and a_{SiO2} are thermodynamic activities of MgO and SiO_2 in the melt, and γ_{Mg} and γ_{SiO} are evaporation coefficients of $Mg_{(g)}$ and $SiO_{(g)}$.

Evaporation of Mg and Si from the same CMAS melt into hydrogen-rich gas depends on hydrogen partial pressure P_{H_2} (e.g., Tsuchiyama et al., 1999; Grossman et al., 2000; Richter et al., 2002). At very low P_{H_2}, the presence of H_2 essentially does not affect partial pressures of major evaporating species (Mg, SiO, O_2) and thus evaporation of CMAS melt occurs via reactions (8) and (9) as in vacuum. At higher P_{H_2} hydrogen acts as a reducing agent such that evaporation of Mg and Si from the melt is now controlled by:

$$MgO_{(melt)} + H_{2(g)} \rightarrow Mg_{(g)} + H_2O_{(g)} \quad (11)$$

$$SiO_{2(melt)} + H_{2(g)} \rightarrow SiO_{(g)} + H_2O_{(g)}. \quad (12)$$

The transitional P_{H_2} between the free vacuum evaporation regime and hydrogen-reaction dominated regime depends on the composition of evaporating material and on temperature, and is estimated to be P_{H_2} ~1×10^{-7} bar at 1727°C (Grossman et al., 2000) and ~3×10^{-8} bar at 1500°C (Richter et al., 2002) for CAI-like melts, and ~4×10^{-6} bar at 1700°C (Tsuchiyama et al., 1999) and ~2×10^{-8} bar at 1535°C (Takigawa et al., 2009) for crystalline forsterite. In the H_2-reaction regime the saturation vapor pressures of $Mg_{(g)}$ and $SiO_{(g)}$ above CMAS melt are expected to increase with increase of P_{H_2} of the surrounding gas as a function of $\sqrt{P_{H2}}$. However, at sufficiently high P_{H_2} ($\geq 10^{-3}$ bar at 1500°C, Richter et al., 2002) recondensation of evaporating gas starts to take place which then reverses $\sqrt{P_{H2}}$ dependence of the evaporation rate on P_{H_2}. Taking into account dependences of evaporation rates J_{Mg} and J_{Si} on P_{H_2}, one would expect that evaporation rates at 2×10^{-4} bar H_2 should be 3.2 times faster than at 2×10^{-5} bar H_2 and ~45 times faster than in vacuum (assuming that the transitional P_{H_2} for CAI4B2 melt at 1600°C is 1×10^{-7} bar H_2). Similarly, J_{Mg} and J_{Si} at 2×10^{-5} bar are expected to be 15 times faster than in vacuum. These relative rates are close to those which we calculate from our experiments (Section 4.1):

evaporation rates at 2×10^{-4} bar H_2 are ~2.8 times faster than at 2×10^{-5} bar and ~45 times faster than in vacuum; evaporation rates at 2×10^{-5} bar H_2 are ~16 times faster than in vacuum.

In the H_2–reaction-dominated regime, an increase of P_{H_2} results in an increase of both P_{Mg} and P_{SiO}; therefore, the relative evaporation rates of Mg and Si (J_{Mg} / J_{Si}) from the melt at a given temperature are expected to follow relationship (10) and be the same both in vacuum and low-P_{H_2} conditions. This would imply that evaporation trajectories of CMAS melts will be very similar. This is now confirmed by our evaporation experiments in vacuum, at 2×10^{-4} and 2×10^{-5} bar H_2.

The relationship (10) shows that relative evaporation rates of Mg and Si strongly depend on activities of SiO_2 and MgO in the melts and evaporation coefficients of $Mg_{(g)}$ and $SiO_{(g)}$. For SiO_2-rich CMAS melts with $a_{SiO2}/a_{MgO} \gg 1$ (as in CAIB of Richter et al., 2007), saturation vapor pressure P_{SiO} will be higher than P_{Mg} which, in the case of $\gamma_{SiO} \sim \gamma_{Mg}$, would cause faster evaporation of Si relative to Mg and thus result in a faster decrease in a_{SiO2}. When activities of SiO_2 and MgO in the residual melt becomes comparable, P_{SiO} and P_{Mg} will also be close, resulting in $J_{Mg} \sim J_{Si}$. Further decrease of starting a_{SiO2} would cause the residual melt to be enriched in MgO ($a_{SiO2}/a_{MgO} \ll 1$) such that P_{Mg} will be higher than P_{SiO} causing faster evaporation of Mg relative to Si until P_{SiO} and P_{Mg} become close again and thus $J_{Mg} \sim J_{Si}$. Such an oscillation around a fixed P_{SiO} / P_{Mg} ratio would cause the relative evaporation rates J_{Mg}/J_{Si} to remain constant until near-complete evaporation of one of the components. This would also result in a linear correlation of wt% MgO and SiO_2 lost (as shown in Fig. 4 for CAI4B2, as well as CAIB melts, once ~40 mol% Mg and ~50 mol% Si had evaporated).

Chemical evaporation trajectories for CAI-like CMAS melts that show how chemical composition of the melt evolves during evaporation can also be modeled thermodynamically if evaporation coefficients and activities of melt components are accurately known. Unfortunately, no accurate activity data are available for CAI-like melts, from which evaporation coefficients could be calculated using the evaporation kinetics of Mg and Si from the free evaporation experiments. A common way of obtaining a_i (and thus $P_{i,sat}$) and γ_i is: 1) calculating a_i and $P_{i,sat}$ using a thermodynamic model for a multicomponent silicate melts (such as the CMAS model of Berman, 1983); 2) obtaining γ_i values by fitting the evaporative rates determined from free-surface evaporation experiments and those calculated using $P_{i,sat}$ and Eq. 2 and 3. We emphasize that such an approach requires availability of experimentally measured evaporation rates for a given composition melt at a given temperature, and that the thermodynamic model of liquid used to calculate a_i is accurate. Use of a different thermodynamic model to calculate the properties of the melt might result in different γ_{SiO} and γ_{Mg} and thus evaporation trajectories. For example, Richter et al. (2007) found that different γ_{SiO}/γ_{Mg} at different temperatures are required to fit evaporation trajectories of Type B CAI-like melt (e.g., ~0.88 at 1900°C and 1.35 at 1600°C); Mendybaev et al. (2017) noted that the $\gamma_{SiO}/\gamma_{Mg} \sim 0.4$ at 1900°C is needed to fit the experimental and calculated (using the same CMAS model) evaporation trajectories for forsteritic melts. It remains unclear if these variations of γ_{SiO}/γ_{Mg} on temperature and melt compositions are real, or just reflect inaccuracy of the CMAS model in predicting activities of components for melilitic and forsteritic melts. We should note that good agreement between experimental and calculated chemical evaporation trajectories was observed when thermodynamic model of Shornikov

(2019) with γ_{SiO}/γ_{Mg} =1 for different melts at different temperatures was used (e.g., Mendybaev et al., 2018, 2020).

Available extensive experimental datasets on evaporation of various CAI-like melts under different conditions should be used for further testing and optimization of thermodynamic models.

7. EXPERIMENTAL CONSTRAINTS ON EVAPORATION OF CAI PRECURSORS IN SOLAR NEBULA

Evaporation experiments using non-FUN FoB-like CAI4B2 melt show that the chemical and isotopic evaporation trajectories of magnesium and silicon in low-P_{H_2} gas at 1600°C remain the same as in vacuum, with evaporation kinetics at 2×10^{-5} and 2×10^{-4} bars H_2 being ~16 and ~45 times, correspondingly, faster than in vacuum. Faster kinetics in H_2-rich gas significantly reduces the duration of processes required to produce depletion of moderately volatile magnesium and silicon and their heavy isotope enrichments in natural CAIs. Figure 9 and Table 3 shows such timescales for a 2.5 mm CAI4B2 droplet evaporating at 1500° and 1600°C in solar nebula gas with P_{H_2} of 2×10^{-4} and 2×10^{-5} bars. The curves in Fig. 9 were calculated using our experimentally determined evaporation rates at 1600°C and those reported by Richter et al. (2002) for BCAI melt evaporated at 1500°C and $P_{H_2}=2\times10^{-4}$ bar. We also used the isotopic fractionation factors $\alpha_{25,24}$ = 0.9877 and $\alpha_{25,24}$ = 0.9910 reported above. Also shown in Fig. 9 are the magnesium and silicon elemental depletions and δ^{25}Mg and δ^{29}Si compositions in "normal" coarse-grained Type A and Type B CAIs (Grossman et al., 2008), and in the most fractionated FUN and Type F CAIs (e.g., Mendybaev et al., 2017 and references therein). According to Fig. 9a, it would take less than an hour at 1600°C and 2×10^{-4} bar H_2, two hours at 2×10^{-5} bar H_2, and four hours at 1500°C and 2×10^{-5} bar H_2 to completely evaporate magnesium from the 2.5 mm CAI4B2 droplet. The corresponding timescales for silicon (Fig. 9c) are one, three and about eight hours. The panels *a* and *c* in Fig. 9 and Table 3 also show that it would take only less than 15–25 minutes to deplete Mg and Si to the levels typical for Type A and B coarse-grained CAIs by evaporation of CAI4B2 melt at 1600°C and 2×10^{-4} bar H_2. The timescales would increase to ~0.5–1 hour at 2×10^{-5} bar H_2, and to ~1.5–2 hours if the droplet has evaporated at 1500°C and 2×10^{-4} bar H_2. The corresponding timescales to produce the Mg and Si isotopic fractionations measured in "normal" CAIs (δ^{25}Mg up to 10‰ and δ^{29}Si up to 4‰) would be ~20–25 minutes, ~ 1 hour and ~2–2.5 hours. Panels *b* and *d* also show that it would take $\sim$1 hour at 1600°C and 2×10^{-4} bar H_2, and $\sim$2 hour at 1600°C and 2×10^{-5} bar H_2 to fractionate Mg and Si isotopes up to δ^{25}Mg ~30–35‰ and δ^{29}Si ~10–15‰, comparable to those of the most fractionated Type F and FUN CAIs. Evaporation of a CAI4B2 droplet at 1500°C and 2×10^{-4} bar H_2 for four hours, after which all magnesium will be lost (Fig. 9a), would produce δ^{25}Mg ~30–35‰ but only δ^{29}Si ~7‰. Significantly more Mg-rich (forsteritic) CAI precursors are required to produce residues with δ^{25}Mg ~30–35‰ and δ^{29}Si ~10–15‰ in the latter case. The increase in wt% MgO, and thus decrease in wt% SiO_2, would decrease the fraction of Mg and increase the fraction of Si evaporated which would result in shifting the δ^{25}Mg curve in Fig. 9b toward longer timescales and the δ^{29}Si curve in Fig. 9d toward shorter timescales.

A number of astrophysical models for CAI formation have been proposed, including the high-temperature processing of CAI precursors in the vicinity of the young sun, or during local

high energetic heating events elsewhere. According to the model of Shu and co-authors (e.g., Shu et al., 1996, 2001), aggregates of CAI precursor materials were transported close to the protosun (<0.1 AU), heated to different degrees, and molten droplets were then transported out into the asteroid belt by the X-wind. Unfortunately, the model does not explicitly provide P-T history (peak temperature, duration of heating, cooling rate), but it estimates the peak temperature in the outflow to be around 1525°C or more for a few hours. The cooling rate of molten droplets in the outflow is about 10°C h^{-1} as estimated by Desch et al. (2010) using data of Shu et al. (1996). Although these timescales are comparable with timescales required to produce enrichments of residual melts in heavy Mg, Si and O isotopes (Fig. 9), the model was criticized for internal inconsistencies and discrepancies of the model predictions for CAI and chondrule formation and meteoritic observations (Desch et al., 2010).

There are a number of possible mechanisms that could result in intensive short duration heating and melting of solid particles (hours to days) in highly localized transient heating events in the protoplanetary disk. The igneous texture of coarse-grained CAIs could have been formed essentially in the same processes that resulted in chondrule formation: lightning (e.g., Desch and Cuzzi, 2000); nebular shocks (e.g., Desch and Connolly, 2002; Desch et al., 2010; Morris and Desch, 2010; Morris et al., 2012), current sheets (Hubbard et al., 2012; McNally et al., 2014), collision of planetesimals (e.g., Sanders and Scott, 2012; Johnson et al., 2014), among the others. The shock wave models are probably the most developed ones for chondrule formation and provide sufficiently detailed thermal evolution of reheated silicate grains to compare (favorably) to the results of laboratory experiments on chondrule formation (e.g., Hewins et al., 2005). According to the "canonical" shock model of Desch and Connolly (2002), chondrule precursor materials 0.5 mm in size in such a shock (7 km s^{-1}, pre-shock temperature 25°C and pressure 10^{-5} bar) could be heated by the hot shock front to ~1650°C in a few hours, followed by very fast (minutes) cooling to ~1450°C and slower cooling (35–50°C hr^{-1}) to ~950°C. The model predicts a pressure increase from 10^{-5} bar in front of the shock to ~5×10^{-4} bar after the passage of the shock. Close P-T histories were obtained in model calculations of Morris and Desch (2010) using different shock parameters. The comparable timescales of heating and cooling in nebular shock models and the timescales shown in Fig. 9 allow us, following Richter et al. (2006), to consider the nebular shock events as a very likely mechanism of formation of igneous CAIs with their several permil enrichments in heavy Mg and Si isotopes.

Richter et al. (2006) showed that the chemical and isotopic compositions of melilite crystallized from Type B CAI-like melt agree with the thermal history of a nebular shock model (i.e., Desch and Connolly, 2002). The cooling rates suggested by the model are within the range of the rates needed to form coarse-grained textures of Type B CAIs (0.5 to 50°C h^{-1}), following the laboratory experiments on crystallization of synthetic CAI-like melts (e.g., MacPherson et al., 1984; Stolper and Paque, 1986; Mendybaev et al., 2006a). When similar composition melt cools in hydrogen-rich gas, a melilite mantle typical for Type B1 CAIs forms (Mendybaev et al., 2006a; Kamibayashi et al., 2019); melting and cooling under oxidizing conditions (log fO2 > IW-5, Mendybaev et al., 2006a) or at a very low hydrogen pressures (Kamibayashi et al., 2019), a Type B2-like texture without a melilite mantle forms. These experiments suggest that formation of the melilite mantle of B1 CAIs is caused by the depletion of the outer parts of the droplet in Mg and Si due to a faster evaporation of Mg and Si from the surface of the droplet, compared to their re-supply from the inner parts of the droplet to the surface by diffusion. The latter would homogenize the chemical composition of the droplet. Depletion in Mg and Si would

cause crystallization of more gehlenitic melilite at the outer parts of the droplet first, followed by crystallization of more åkermanitic melilite (and pyroxene and anorthite) in the central parts. We should note, however, that there is a nucleation barrier of melilite crystallization from CMAS melt that is heated above liquidus for extended period of time (e.g., Stolper and Paque, 1986; Mendybaev et al., 2006a) which results in crystallization of dendritic melilite at temperatures much lower than the equilibrium crystallization temperatures. In the absence of the nucleation barrier, euhedral melilite grains typical for igneous CAIs would form (e.g., Beckett, 1986; Stolper and Paque, 1986; Mendybaev et al., 2006a).

Although the P-T history in nebular shocks were used mostly to model formation of chondrules, which are typically about several tenths of millimeters in size, we do not expect that the thermal histories would change dramatically for larger (few millimeters typical for CAIs) droplets. However, in the case of a centimeter- or even several centimeter-size refractory droplets, such as some FUN CAIs, very short heating to 1650°-1700°C might not be enough to completely melt and homogenize the CAI precursor. Evaporation of a large partially molten droplet might be diffusion-controlled and would result in chemically and isotopically zoned FUN CAIs (e.g., Esat et al., 1979; Davis et al., 1991; Krot et al., 2014; Park et al., 2017; Williams et al., 2017; Kööp et al., 2018).

It remains unclear if shocks have acted at the times needed to melt CAIs, and if they have been identical to the ones that melted chondrules (Desch et al., 2010). It is important that nebular shock or any other astrophysical models for CAI formation need to reproduce the short timescales required to produce the observed depletion of coarse-grained CAIs in Mg and Si, and their enrichments in heavy isotopes. The experimental results reported in this paper provide a stringent test of proposed astrophysical models for the origin and evolution of CAIs.

8. CONCLUSIONS

Chemical and isotopic fractionations obtained in low-pressure H_2 (2×10^{-4} and 2×10^{-5} bar H_2) and vacuum evaporation experiments at 1600°C using the same non-FUN FoB CAI-like melt showed that:

1) Although magnesium and silicon evaporate at 2×10^{-4} bar H_2 ~2.8 times faster than at 2×10^{-5} bar H_2 and ~45 times faster than in vacuum, their relative evaporation rates remain the same in all experiments;

2) The isotopic fractionation factors of magnesium and silicon caused by their evaporation from the melt are the same in vacuum and low-P_{H_2} gas, with fractionation factors for Mg isotopes of $\alpha_{25,24} = 0.9877\pm0.0004$ and Si isotopes of $\alpha_{29,28} = 0.9910\pm0.0005$; the values of $\alpha_{25,24}$ and $\alpha_{29,28}$ are the same as obtained in previous studies for melilitic melts at 1600°C;

3) The relative evaporation rates of magnesium and silicon and their isotopic fractionation factors are independent of hydrogen pressure in the surrounding gas, which results in the same chemical and isotopic evolution trajectories in vacuum and low-P_{H_2} gas;

4) Very short timescales (20–25 minutes at 1600°C and 2×10^{-4} bar H_2, ~ 1 hour at 1600°C and 2×10^{-5} bar H_2 and 2–2.5 hours at 1500°C and 2×10^{-4} bar H_2) are required to produce δ^{25}Mg up to ~ 10‰ and δ^{29}Si up to ~ 4‰, typical for "normal" coarse-grained Type A and

B CAIs. The timescales will increase by a factor of two to fractionate magnesium and silicon isotopes up to δ^{25}Mg ~30–35‰ and δ^{29}Si ~10–15‰ as in the most fractionated Type F and FUN CAIs. The short timescales suggest melting and evaporation of CAI precursors in very short dynamic heating events;

5) Any astrophysical model that predicts rapid processing of CAI precursors (e.g., X-wind, shock waves, current sheets; etc.) has to reproduce the very short timescales required to produce the observed depletion of coarse-grained CAIs in Mg and Si, and enrichment in their heavy isotopes.

ACKNOWLEDGMENTS

The authors thank Dimitri Papanastassiou (AE), Denton Ebel and two anonymous reviewers for their comments and suggestions which improved this paper. We are also grateful to Andrew Davis for reading the paper and his suggestions. This work was supported by NASA grant NNX17AE84G (to R.M.). Magnesium isotopic measurements were supported by NSF grant EAR-17407706 (to F.-Z. T.). P.S. and the Si isotope measurements made at the St Andrews Isotope Group (STAiG) at the University of St Andrews were supported by NERC grant NE/R002134/1 a Carnegie Trust Research Incentive Grant. Evaporation experiments at Hokkaido University were supported by the Ministry of Education, Sports, Science, and Technology KAKENHI Grant (to S.T.).

REFERENCES:

Amelin Y., Kaltenbach A., Iizuka T., Stirling C. H., Ireland T. R., Petaev M., and Jacobsen S. B. (2010) U-Pb chronology of the Solar System's oldest solids with variable $^{238}U/^{235}U$. *Earth Planet. Sci. Lett.* **300**, 343–350.

Beckett J. R. (1986) The origin of calcium-, aluminum-rich inclusions from carbonaceous chondrites: an experimental study. Ph.D. thesis, University of Chicago.

Berman R. G. (1983) A thermodynamic model for multicomponent melts, with application to the system CaO-MgO-Al_2O_3-SiO_2. Ph. D. thesis, University of British Columbia.

Bouvier A. and Wadhwa (2010) The age of the Solar System redefined by the oldest Pb-Pb age of a meteoritic inclusion. *Nature Geosci.* **3**, 637–641.

Bullock E. S., MacPherson G. J., Nagashima K., Krot A. N., Petaev M. I., Jacobsen S. B., and Ulyanov A. A. (2012) Forsterite-bearing type B refractory inclusions from CV3 chondrites: From aggregates to volatilized melt droplets. *Meteoritics & Planetary Science* **47,** 2128–2147.

Connelly J. N., Bizzarro M., Krot A. N., Nordlund A., Wielandt D., and Ivanova M. A. (2012) The absolute chronology and thermal processing of solids in the solar protoplanetary disk. *Science* **338**, 651–655.

Costa G.C., Jacobson N.S., and Fegley B. Jr. (2017) Vaporization and thermodynamics of forsterite-rich olivine and some implications for silicate atmospheres of hot rocky exoplanets. *Icarus* **289**, 42–55.

Davis A. M., Hashimoto A., Clayton R. N., and Mayeda T. K. (1990) Isotope mass fractionation during evaporation of Mg_2SiO_4. *Nature* **347**, 655–658.

Davis A. M., MacPherson G. J., Clayton R. N., Mayeda T. K., Sylvester P. J., Grossman L., Hinton R. W. and Laughlin J. R.(1991) Melt solidification and late-stage evaporation in the evolution of a FUN inclusion from the Vigarano C3V chondrite. *Geochim. Cosmochim. Acta* **55**, 621–637.

Desch S. J. and Connolly H. C., Jr. (2002) A model of the thermal processing of particles in solar nebula shocks: Application to the cooling rates of chondrules. *Meteorit. Planet. Sci.* **37**, 183–202.

Desch S. J. and Cuzzi J. N. (2000) Generation of lightning in the solar nebula. *Icarus* **143**, 87–105.

Desch S.J., Morris M.A., Connolly H.C., and Boss A.P. (2010) A critical examination of the X-wind model for chondrule and calcium-rich, aluminum-rich inclusion formation and radionuclide production. *Astrophys. J.* **725,** 692–711.

Ebel D.S. and Grossman L. (2000) Condensation in dust-enriched systems. *Geochim. Cosmochim. Acta* **64**, 339–366.

Esat T. M., Papanastassiou D. A., and Wasserburg G. J. (1979) Trials and tribulations of ^{26}Al: Evidence for disturbed systems. *13th Lunar. Planet. Sci.*, Lunar Planet. Inst., Houston, 361–363 (abstr.).

Floss C., El Goresy A., Zinner E., Kransel G., Rammensee W., Palme H. (1996) Elemental and isotopic fractionations produced through evaporation of the Allende CV chondrite:

Implications for the origin of HAL-type hibonite inclusions. *Geochim. Cosmochim. Acta* **60**, 1975–1997

Georg R. B., Reynolds B. C., Frank M., and Halliday A. N. (2006) New sample preparation techniques for the determination of Si isotopic composition using MC-ICPMS. *Chem. Geol.* **235**, 95–104.

Grossman L., Ebel D. S., Simon S. B., Davis A. M., Richter F. M., and Parsad N. M. (2000) Major element chemical and isotopic compositions of refractory inclusions in C3 chondrites: the separate roles of condensation and evaporation. *Geochim. Cosmochim. Acta* **64**, 2879–2894.

Grossman L., Simon S. B., Rai V. K., Thiemens M. H., Hutcheon I. D., Williams R. W., Galy A., Ding T., Fedkin A. V., Clayton R. N., Mayeda T. K. (2008) Primordial composition of refractory inclusions. *Geochim. Cosmochim. Acta* **72**, 3001–3021.

Hashimoto A. (1990) Evaporation kinetics of forsterite and implications for the early solar nebula. *Nature* **347**, 53–55.

Hewins R. H., Connolly H. C. Jr., Lofgren G. E., and Libourel G. (2005) Experimental constraints on chondrule formation. In *Chondrites and the protoplanetary disk (*A. N. Krot, E. R. D. Scott, and B. Reipurth, eds.), Astronom. Soc. Pacific, San Francisco, CA, 286–316.

Hirth J. P. and Pound G. P. (1963) Condensation and evaporation. Nucleation and growth kinetics. Macmillan, New York, 191 p.

Hubbard A., McNally C. P., and Mac Low M.-M. (2012) Short circuits in thermally ionized plasmas: A mechanism for intermittent heating of protoplanetary disks. *Astrophys. J.* **761,** #58 (10pp).

Ivanova M. A., Mendybaev R. A., Shornikov S. I., Ryazantsev K. M., and MacPherson G. J. (2018) Evaporation of spinel-rich CAI melts: A possible link to CH-CB CAIs. *49th Lunar. Planet. Sci.*, Lunar Planet. Inst., Houston. #1965 (abstr.).

Johnson B. C., Minton D. A., Melosh H. J., Zuber M. T. (2014) Impact jetting as the origin of chondrules. *Nature* **517**, 339–341.

Kamibayashi M., Yamamoto D., Tachibana S., and Yurimoto H. (2019) Crystallization of Type B CAI melt in low-pressure hydrogen gas and implication for formation conditions of igneous CAIs. *82nd Annu. Meteorit. Soc. Meet.*, #6254 (abstr.).

Knight K. B., Kita N. T., Mendybaev R. A., Richter F. M., Davis A. M., and Valley J. W. (2009) Silicon isotope fractionation of CAI-like vacuum evaporation residues. *Geochim. Cosmochim. Acta* **73**, 6390–6401.

Kööp L., Nakashima D., Heck P. R., Kita N. T., Tenner T. J., Krot A. N., Nagashima K., Park C., Davis A. M. (2018) A multielement isotopic study of refractory FUN and F CAIs: Mass-dependent and mass-independent isotope effects. *Geochim. Cosmochim. Acta* **221**, 296–317.

Krot A. N. (2019) Refractory inclusions in carbonaceous chondrites: Records of early solar system processes. *Meteorit. Planet. Sci.* **55**, 1–45.

Krot A. N., Nagashima K., Wasserburg G. J., Huss G. R., Papanastassiou D., Davis A. M., Hutcheon I. D., Bizzarro M. (2014) Calcium-aluminum-rich inclusions with fractionation and unknown nuclear effects (FUN CAIs): I. Mineralogy, petrology, and oxygen isotopic compositions. *Geochim. Cosmochim. Acta* **145**, 206–247.

Lange R. A. and Carmichael I. S. E. (1987) Densities of Na_2O–K_2O–CaO–MgO–FeO–Fe_2O_3–Al_2O_3–TiO_2–SiO_2 liquids: new measurements and derived partial molar properties. *Geochim. Cosmochim. Acta* **51**, 2931–2946.

MacPherson G. J. (2014) Calcium-aluminum-rich inclusions in chondritic meteorites. In *Meteorites, and Cosmochemical Processes* (*A. M. Davis, ed.*), *Treatise on Geochemistry* (second edition), 1. (H. D. Holland and K. K. Turekian, eds), Elsevier, Amsterdam, 139–179.

MacPherson G. J., Paque J. M., Stolper E., and Grossman L. (1984) The origin and significance of reverse zoning in melilite from Allende Type B inclusions. *J. Geol.* **92**, 289-305.

McNally C. P., Hubbard A., Yang C.-C., and Mac Low M.-M. (2014) Temperature fluctuations driven by magnetorotational instability in protoplanetary disks. *Astrophys. J.* **791,** #62 (15pp).

Mendybaev R. A. and Richter F. M. (2016) Chemical and isotopic fractionation during evaporation of AOA- and FoB-like materials. *47th Lunar Planet. Sci.,* Lunar Planet. Inst., Houston. #2929 (abstr.).

Mendybaev R. A. and Shornikov S. I. (2018) Evaporation of CaO-MgO-Al_2O_3-SiO_2 melts: Experimental and thermodynamic modeling. (2018) *81st Annu. Meteorit. Soc. Meet*. #2067 (abstr.).

Mendybaev R. A., Richter F. M., and Davis A. M. (2006a) Crystallization of melilite from CMAS-liquids and the formation of the melilite mantle of Type B1 CAIs: Experimental simulations. *Geochim. Cosmochim. Acta* **70***,* 2622–2642.

Mendybaev R. A., Richter F. M., and Davis A. M. (2006b) Reevaluation of the åkermanite-gehlenite binary system. *37th Lunar Planet. Sci.,* Lunar Planet. Inst., Houston. #2268 (abstr.)

Mendybaev R. A., Richter F. M., Georg R. B., Janney P. E., Spicuzza M. J., Davis A. M., Valley J. W. (2013a) Experimental evaporation of Mg- and Si-rich melts: implications for the origin and evolution of FUN CAIs. *Geochim. Cosmochim. Acta* **123**, 368–384.

Mendybaev R. A., Teng F.-Z. Georg R. B., and Richter F. M. (2013b) Magnesium and silicon isotopic fractionations during evaporation of forsterite-rich melts. *44th Lunar Planet. Sci.,* Lunar Planet. Inst., Houston. #3017 (abstr.).

Mendybaev R. A., Williams C. D., Spicuzza M. J., Richter F. M., Valley J. W., Fedkin A. V., Wadhwa M. (2017) Thermal and chemical evolution in the early Solar System as recorded by FUN CAIs: Part II - Laboratory evaporation of potential CMS-1 precursor material. *Geochim. Cosmochim. Acta* **201**, 49–64.

Mendybaev R. A., Shornikov S. I., Jacobson N. S., and Kowalski B. (2020) Thermodynamics and evaporation kinetics of CAI-like melts. *51st Lunar. Planet. Sci.*, Lunar Planet. Inst., Houston. #2168 (abstr.).

Morris M. A. and Desch S. J. (2010) Thermal histories of chondrules in solar nebula shocks. *Astrophys. J.* **722**, 1474–1494.

Morris M. A., Boley A. C., Desch S. J., and Athanassiadou T. (2012) Chondrule formation in bow shocks around eccentric planetary embryos. *Astrophys. J.* **752, #**27 (17 pp).

Osborn E. F. and Schairer J. F. (1941) The ternary system pseudo-wollastonite-åkermanite-gehlenite. *Amer. J. Sci*. **231**, 715–763.

Park C., Nagashima K., Krot A. N., Huss G. R., Davis A. M., Bizzarro M. (2017) Calcium-aluminum-rich inclusions with fractionation and unidentified nuclear effects (FUN CAIs): II.

Heterogeneities of magnesium isotopes and ^{26}Al in the early Solar System inferred from *in situ* high-precision magnesium-isotope measurements. *Geochim. Cosmochim. Acta* **201**, 6–24.

Reynolds B. C., Aggarwal J., André L., Baxter D., Beucher C., Brzezinski M. A., Engström E., Georg R. B., Land M., Leng M. J., Opfergelt S., Rodushkin I., Sloane H. J., van den Boorn S. H. J. M., Vroon P. Z. and Cardinal D. (2007) An inter-laboratory comparison of Si isotope reference materials. *J. Anal. Atom. Spectr*. **22**, 561–568.

Richter F. M., Davis A. M., Ebel D. S., and Hashimoto A. (2002) Elemental and isotopic fractionation of Type B calcium-, aluminum-rich inclusions: experiments, theoretical considerations, and constraints on their thermal evolution. *Geochim. Cosmochim. Acta* **66**, 521–540.

Richter F. M., Janney P. E., Mendybaev R. A., Davis A. M., and Wadhwa M. (2007) Elemental and isotopic fractionation of Type B CAI-like liquids by evaporation. *Geochim. Cosmochim. Acta* **71**, 5544–5564.

Sanders I. S. and Scott E. R. D. (2012) The origin of chondrules and chondrites: Debris from low-velocity impacts between molten planetesimals. *Meteorit. Planet. Sci*. **47**, 2170–2192.

Savage P. S. and Moynier F. (2013) Silicon isotopic variation in enstatite meteorites: Clues to their origin and Earth-forming material. *Earth Planet. Sci. Letters* **361,** 487–496.

Savage P. S., Armytage R. M. G., Georg R. B., Halliday A. N. (2014) High temperature silicon isotope geochemistry. *Lithos* **190-191**, 500–519.

Shornikov S. I. (2019) Thermodynamic modeling of evaporation processes of lunar and meteorite substance. *Geochem. Internat*. **57** (8), 865–872.

Shornikov S. I. and Yakovlev O. I. (2015) Study of complex molecular species in the gas phase over CaO-MgO-Al_2O_3-TiO_2-SiO_2 system. *Geochem. Internat*. **53**, 690–699.

Shu F. H., Shang H., and Lee T. (1996) Toward an astrophysical theory of chondrites. *Science* **271**, 1545–1552.

Shu F. H., Shang H., Gounelle M., Glassgold A. E., and Lee T. (2001) The origin of chondrules and refractory inclusions in chondritic meteorites. *Astrophys. J.* **548**:1029–1050.

Stolper E. and Paque J. M. (1986) Crystallization sequences of Ca-Al-rich inclusions from Allende: the effects of cooling rate and maximum temperature. *Geochim. Cosmochim. Acta* **50**, 1785–1806.

Takigawa A., Tachibana S., Nagahara H., Ozawa K., and Yokoyama M. (2009) Anisotropic evaporation of forsterite and its implication for dust formation conditions in circumstellar environments. *Astrophys. J. Lett*., **707**, L97–L101.

Teng F.-Z. and Yang W. (2014) Comparison of factors affecting accuracy of high-precision magnesium isotope analysis by MC-ICPMS. *Rapid Comm. Mass Spectrom*. **28**, 19–24.

Teng F.-Z., Li W.-Y., Ke S., Marty B., Dauphas N., Huang S., Wu F.-Y., Pourmand A. (2010) Magnesium isotopic composition of the Earth and chondrites. *Geochim. Cosmochim. Acta* **74**, 4150–4166.

Teng F.-Z., Li W.-Y., Ke S., Yang W., Liu S.-A., Sedaghatpour F., Wang S.-J., Huang K.-J., Hu Y., Ling M.-X., Xiao Y., Liu X.-M., Li X.-W., Gu H.-O., Sio C.K., Wallace D.A., Su B.-X., Zhao L., Chamberlin J., Harrington M., Brewer A. (2015a) Magnesium isotopic

compositions of international geological reference materials. *Geostandards Geoanalyt. Res.* **39**, 329–339.

Teng F.-Z., Yin Q.-Z., Ullmann C. V., Chakrabarti R., Pogge von Strandmann P. A. E., Yang W., Li W.-Y., Ke S., Sedaghatpour F., Wimpenny J., Meixner A., Romer R. L., Wiechert U. and Jacobsen S. B. (2015b) Interlaboratory comparison of magnesium isotopic compositions of 12 felsic to ultramafic igneous rock standards analyzed by MC-ICPMS. *Geochem. Geophys. Geosys.* **16**, 3197–3209.

Trail D., Boehnke P., Savage P. S., Liu M.-C., Miller M., and Bindeman I. (2018) Origin and significance of Si and O isotope heterogeneities in Phanerozoic, Archean, and Hadean zircon. *Proc. Natl. Acad. Sci. USA* **115**, 10287–10292.

Tsuchiyama A., Tachibana S. and Takahashi T. (1999) Evaporation of forsterite in primordial solar nebula; rates and accompanied isotopic fractionation. *Geochim. Cosmochim. Acta* **63**, 2451–2466.

Ustunisik G., Ebel D. S., Walker D., and Boesenberg J. S. (2014) Experimental investigation of condensation predictions in dust-enriched systems. *Geochim. Cosmochim. Acta* **142,** 27-38.

Wang J., Davis A. M., Clayton R. N., Mayeda T. K., and Hashimoto A. (2001) Chemical and isotopic fractionation during the evaporation of the FeO-MgO-SiO_2-CaO-Al_2O_3-TiO_2-REE melt system. *Geochim. Cosmochim. Acta* **65**, 479–494.

Williams C. D., Ushikubo T., Bullock E. S., Janney P. E., Hines R. R., Kita N. T., Hervig R. L., MacPherson G. J., Mendybaev R. A., Richter F. M., and Wadhwa M. (2017) Thermal and chemical evolution in the early Solar System as recorded by FUN CAIs: Part I - Petrology, mineral chemistry, and isotopic composition of Allende FUN CAI CMS-1. *Geochim. Cosmochim. Acta* **201**, 25–48.

Table 1. Experimental conditions, chemical composit

Sample	size, mm	Run duration, min	Initial weight, g	Initial surface area, cm^2
CAI4B2-2	2.5	3	0.01694	0.177
CAI4B2-16	2.5	10	0.03692	0.278
CAI4B2-12	2.5	20	0.03363	0.262
CAI4B2-3	2.5	30	0.01758	0.180
CAI4B2-14	2.5	35	0.03960	0.291
CAI4B2-10	2.5	45	0.03568	0.272
CAI4B2-4	2.5	60	0.01915	0.183
CAI4B2-26	1.5	10	0.00725	0.095
CAI4B2-28	1.5	20	0.00783	0.100
CAI4B2-30	1.5	30	0.00613	0.088
CAI4B2-31	1.5	30	0.00825	0.103
CAI4B2-29	1.5	40	0.00536	0.082
CAI4B2-32	1.5	120	0.00849	0.105
CAI4B2-13	2.5	60	0.04731	0.327
CAI4B2-1	2.5	5	0.02388	0.211
CAI4B2-25	2.5	300	0.01966	0.190
CAI4B2-22	2.5	600	0.02300	0.210
CAI4B2-21	2.5	1200	0.01817	0.183
CAI4B2-23	2.5	1700	0.02542	0.221
CAI4B2-20	2.5	1800	0.01792	0.182
CAI4B2-24	2.5	2100	0.03076	0.247
CAI4B2-18	2.5	2400	0.02003	0.192
CAI4B2-19	2.5	3300	0.02826	0.235

Notes: (1) Percent of Mg and Si lost from the sample by evaporation was calcula

(2) Evaporation rates of Mg and Si in the experiment were calculated usir

Table 2. Isotopic compositions of magnesium and silicon in evapora

Sample	Fraction evaporated		Mg isotopic composition (measu		
	Mg	Si	δ^{25}Mg, ‰	2 std	δ^{26}Mg, ‰
CAI4B2-2	0.031	0.020	-0.97	0.05	-1.90
CAI4B2-16	0.112	0.104	0.04	0.05	0.06
CAI4B2-16 [a)]		*0.104*			
CAI4B2-12	0.292	0.221	2.76	0.05	5.42
CAI4B2-12 [a)]		*0.221*			
CAI4B2-3 [a)]	*0.869*	*0.601*	*19.70*	*0.05*	*38.89*
CAI4B2-14	0.518	0.35	7.18	0.05	14.09
CAI4B2-14 [a)]		*0.35*			
CAI4B2-10 [a)]	*0.747*	*0.486*	*15.12*	*0.05*	*29.81*
CAI4B2-26	0.449	0.337			
CAI4B2-28	0.624	0.432			
CAI4B2-30	1.000	0.974			
CAI4B2-31	0.250	0.148			
CAI4B2-29	0.533	0.406			
CAI4B2-13	0.341	0.251			
CAI4B2-1 [a)]	*0.000*	*0.000*	*-1.66*	*0.05*	*-3.21*
CAI4B2-25	0.105	0.063	0.87	0.06	1.64
CAI4B2-22	0.26	0.150	2.51	0.06	4.89
CAI4B2-21	0.642	0.414	10.90	0.06	21.42
CAI4B2-23	0.832	0.555	20.90	0.06	41.51

[1] - Measured Mg and Si isotopic compositions are relative to DSM-3 and NBS28, respectively.

[a)] Shown in italic are Si isotopic composition measured at Trent University.

Note: Fractions of Mg and Si evaporated and isotopic compositions are relative to the sample C

Figure

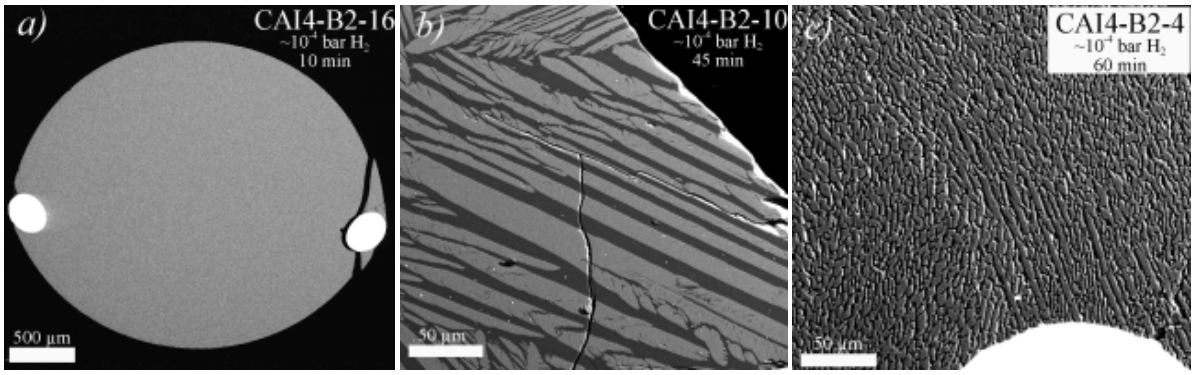

Fig. 1

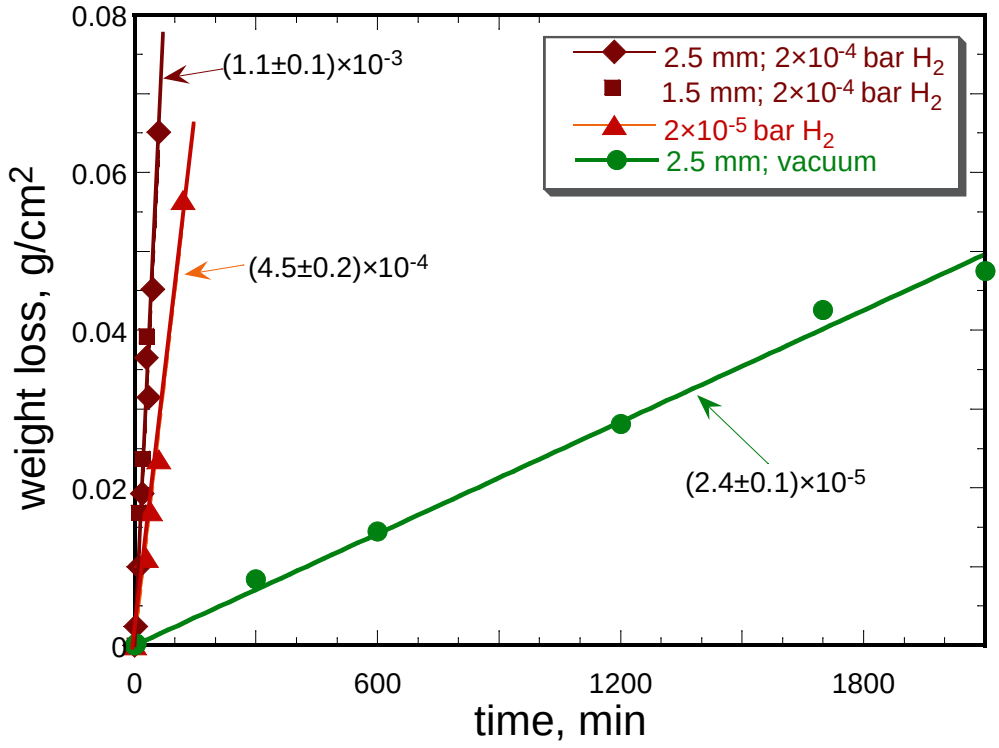

Fig. 2

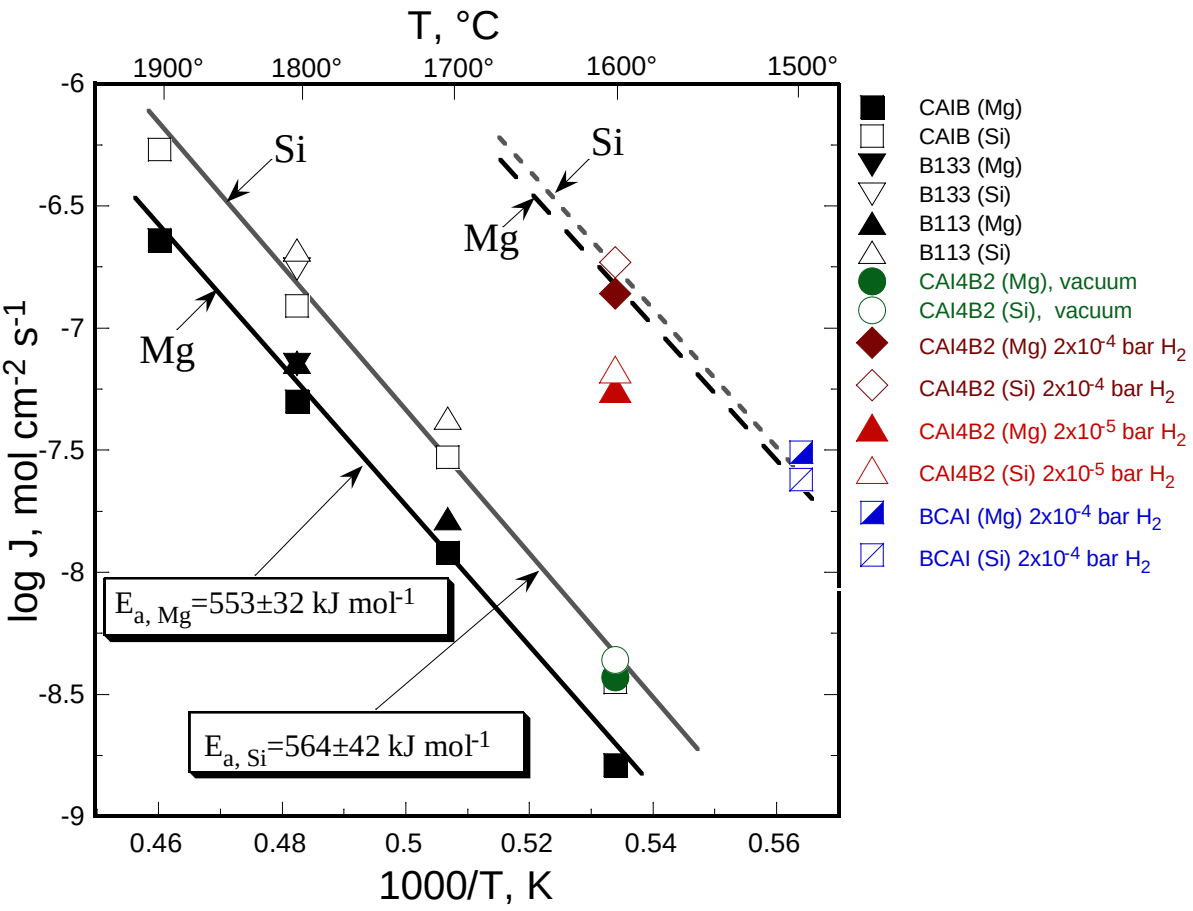
T, °C
1900°
1800°
1700°
1600°
1500°
-6
-6.5
-7
-7.5
-8
-8.5
-9
log J, mol cm-2 s-1
0.46
0.48
0.5
0.52
0.54
0.56
1000/T, K
Si
Mg
Si
Mg
Ea, Mg=553±32 kJ mol-1
Ea, Si=564±42 kJ mol-1
CAIB (Mg)
CAIB (Si)
B133 (Mg)
B133 (Si)
B113 (Mg)
B113 (Si)
CAI4B2 (Mg), vacuum
CAI4B2 (Si), vacuum
CAI4B2 (Mg) 2x10-4 bar H2
CAI4B2 (Si) 2x10-4 bar H2
CAI4B2 (Mg) 2x10-5 bar H2
CAI4B2 (Si) 2x10-5 bar H2
BCAI (Mg) 2x10-4 bar H2
BCAI (Si) 2x10-4 bar H2

Fig. 3

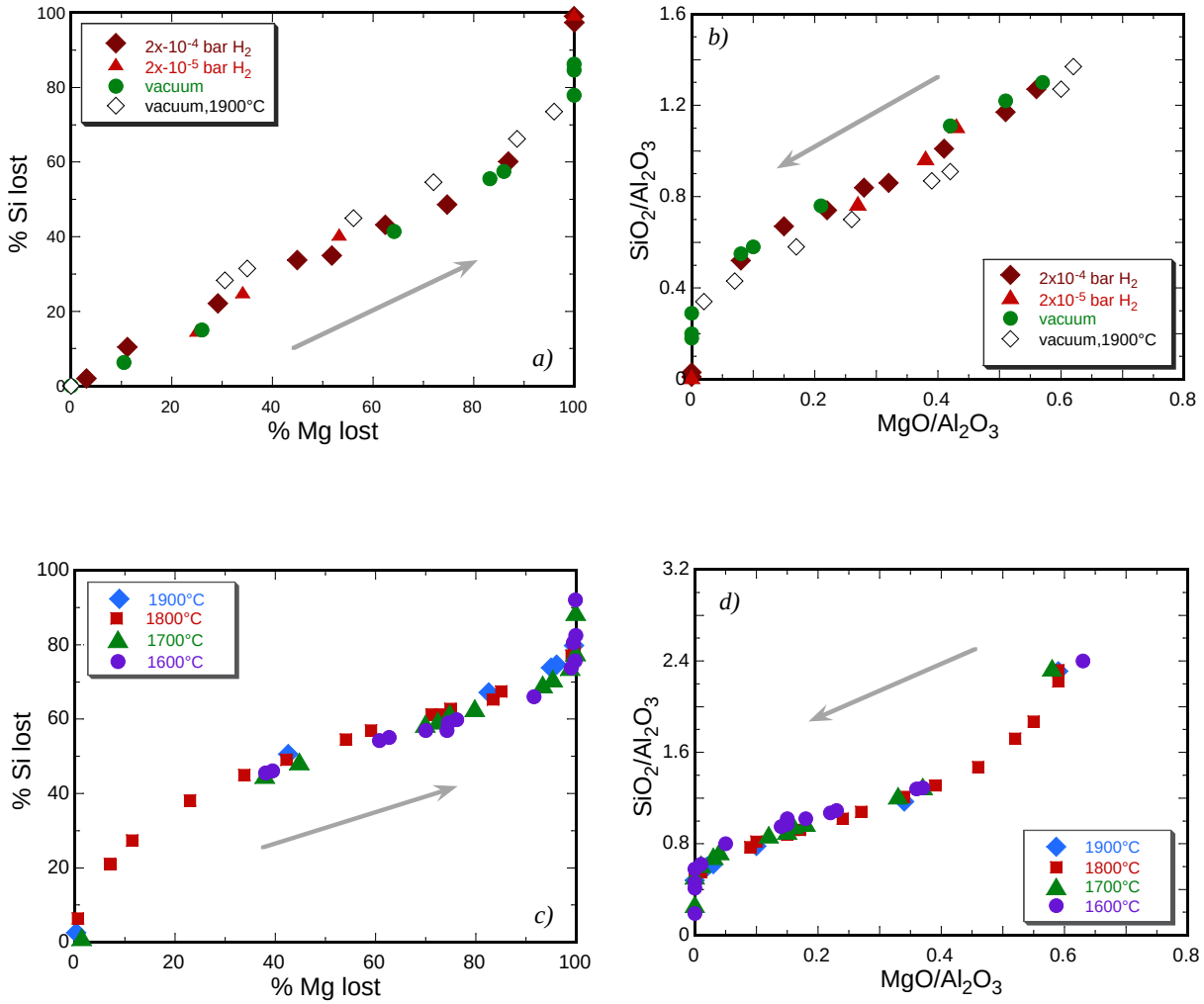
a)
% Si lost
% Mg lost
2x-10-4 bar H2
2x-10-5 bar H2
vacuum
vacuum,1900°C
b)
SiO2/Al2O3
MgO/Al2O3
c)
d)
1900°C
1800°C
1700°C
1600°C

Fig. 4.

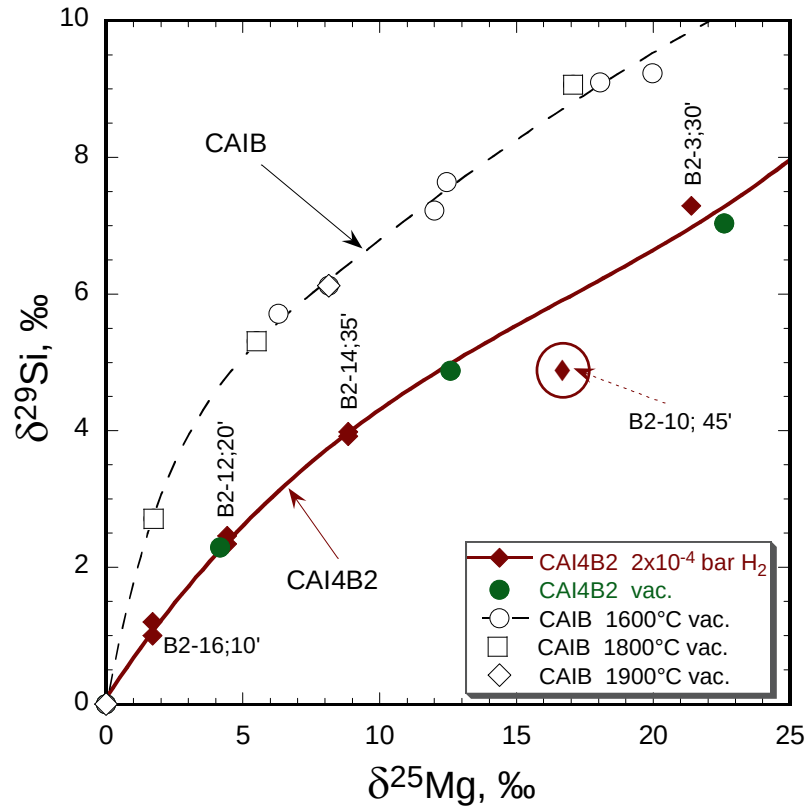
CAIB
B2-3;30'
B2-14;35'
B2-12;20'
B2-10; 45'
CAI4B2
B2-16;10'
CAI4B2 2x10-4 bar H2
CAI4B2 vac.
CAIB 1600°C vac.
CAIB 1800°C vac.
CAIB 1900°C vac.
δ29Si, ‰
δ25Mg, ‰

Fig. 5

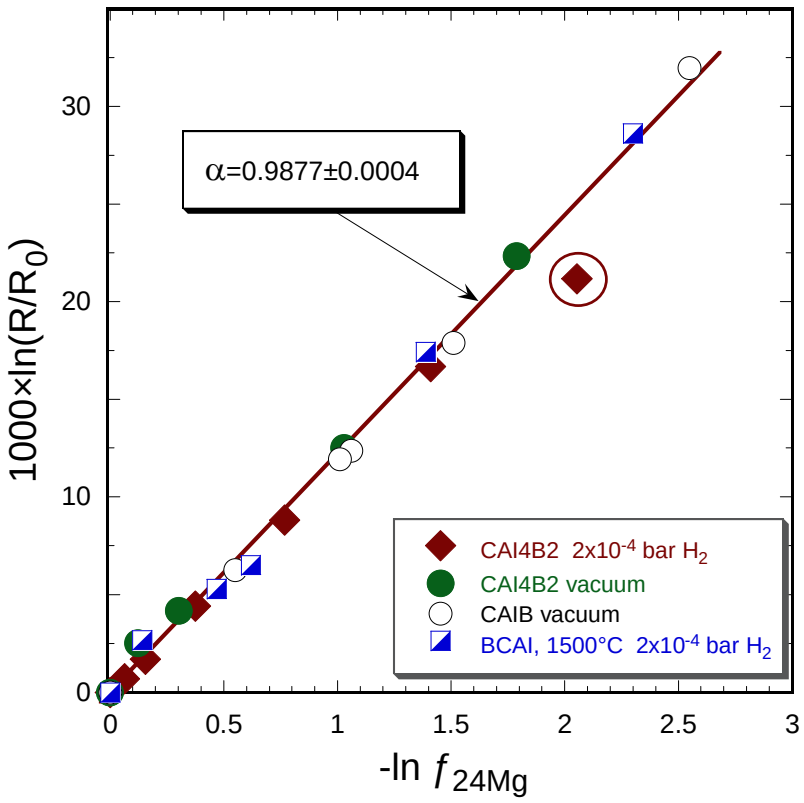
α=0.9877±0.0004
CAI4B2 2x10-4 bar H2
CAI4B2 vacuum
CAIB vacuum
BCAI, 1500°C 2x10-4 bar H2
1000×ln(R/R0)
-ln f 24Mg

Fig. 6

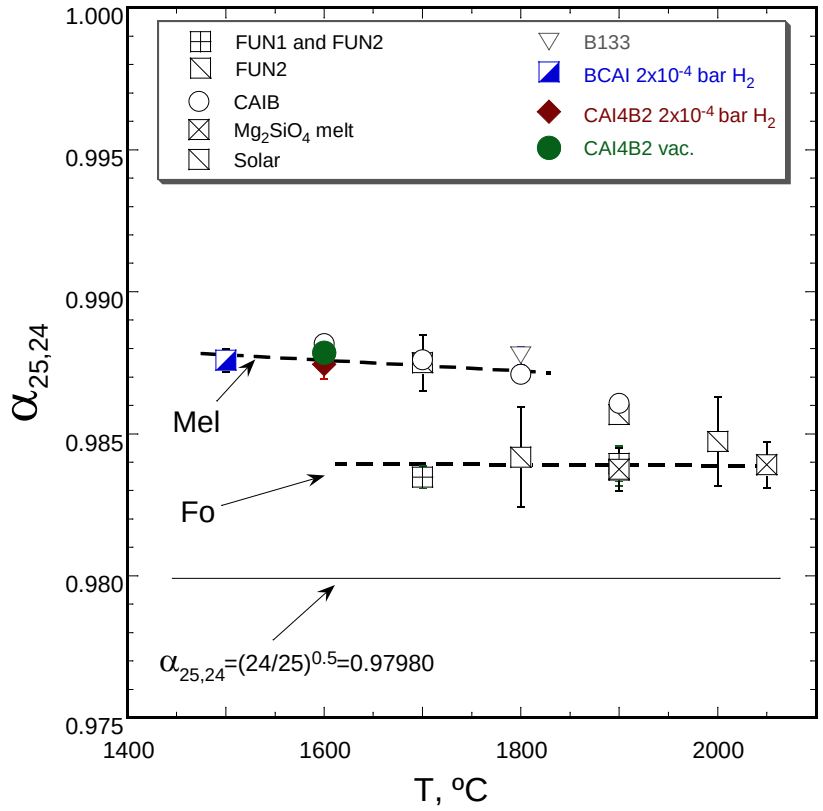
FUN1 and FUN2
FUN2
CAIB
Mg2SiO4 melt
Solar
B133
BCAI 2x10-4 bar H2
CAI4B2 2x10-4 bar H2
CAI4B2 vac.
Mel
Fo
α25,24=(24/25)0.5=0.97980
α25,24
T, ºC

Fig. 7

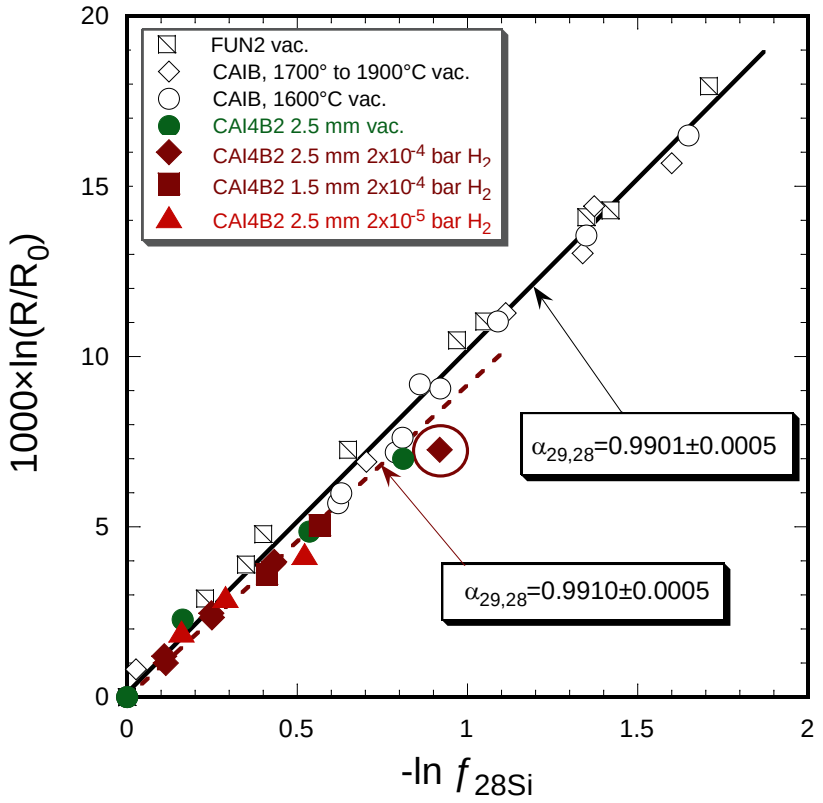
FUN2 vac.
CAIB, 1700° to 1900°C vac.
CAIB, 1600°C vac.
CAI4B2 2.5 mm vac.
CAI4B2 2.5 mm 2x10-4 bar H2
CAI4B2 1.5 mm 2x10-4 bar H2
CAI4B2 2.5 mm 2x10-5 bar H2
α29,28=0.9901±0.0005
α29,28=0.9910±0.0005
1000×ln(R/R0)
-ln f 28Si

Fig. 8

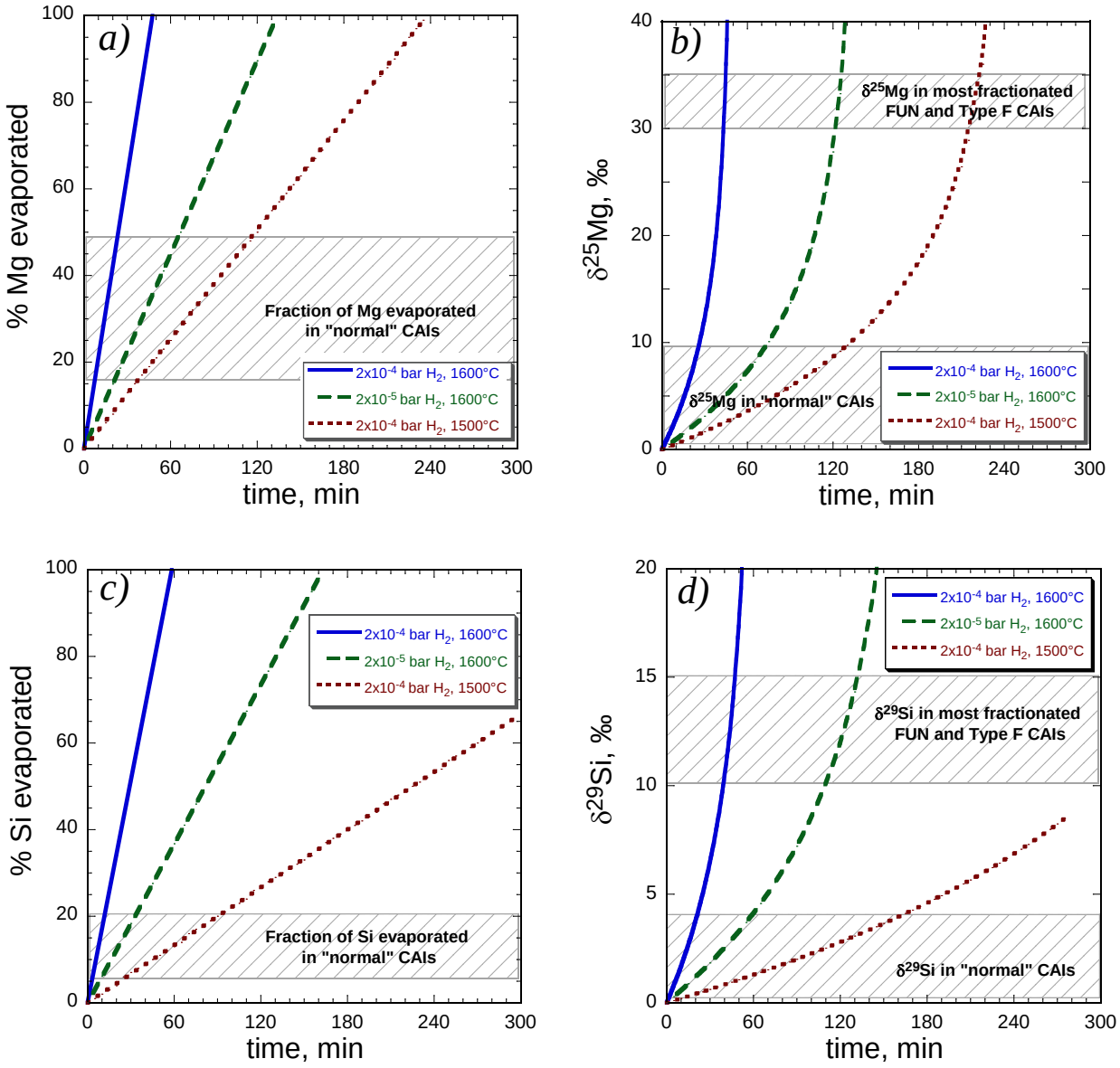
a)
% Mg evaporated
time, min
Fraction of Mg evaporated
in "normal" CAIs
2x10-4 bar H2, 1600°C
2x10-5 bar H2, 1600°C
2x10-4 bar H2, 1500°C
b)
δ25Mg, ‰
time, min
δ25Mg in most fractionated
FUN and Type F CAIs
δ25Mg in "normal" CAIs
c)
% Si evaporated
time, min
Fraction of Si evaporated
in "normal" CAIs
d)
δ29Si, ‰
time, min
δ29Si in most fractionated
FUN and Type F CAIs
δ29Si in "normal" CAIs

Fig. 9.

Figure captions.

Fig. 1. Backscattered electron images of some CAI4B2 evaporation residues. The residues with bulk chemical composition within the melilite stability field appear as a clear glass (panel a; sample B2-16 evaporated for 10 minutes at 2×10^{-4} bar H_2). Samples that lost most of their magnesium and silicon consist mainly of $CaAl_2O_4$ (panel c; sample B2-4 evaporated for 60 minutes at 2×10^{-4} bar H_2). No attempt has been made to identify the Ca-aluminate: krotite or dmitryivanovite. One sample (panel b; sample B2-10) consisted of intergrowth of gehlenitic melilite (gray) and glass(dark). The reason for melilite crystallization most likely due to the actual run temperature being lower than the targetted 1600°C (see text for details).

Fig. 2. Surface area normalized total weight loss of CAI4B2 samples versus run duration at 1600°C: at 2×10^{-4} bar H_2 (diamonds for 2.5 mm and squares for 1.5 mm diameter samples), at 2×10^{-5} bar H_2 (triangles), and in vacuum (circles). Shown evaporation rates of CAI4B2 droplets at 2×10^{-4} bar H_2 and 2×10^{-5} bar H_2 are about 45 and 19 times, respectively, faster than in vacuum.

Fig. 3. Average evaporation rates of magnesium (closed symbols) and silicon (open symbols) from CAI-like melts as a function of temperature. The fit to evaporation data for CAIB (Richter et al., 2007), B133 and B113 (Richter et al., 2002), and CAI4B2 (this study) melts from vacuum experiments results in the activation energy E_a=553±32 kJ mol^{-1} for magnesium evaporation and E_a=564±42 kJ mol^{-1} for silicon evaporation. The dashed lines for 2×10^{-4} bar H_2 experiments with CAI4B2 (this study) and BCAI (Richter et al., 2002) melts were obtained using E_as from the vacuum experiments. Evaporation rates of Mg and Si for CAI4B2 and BCAI melts are very close both in vacuum and at low-P_{H_2} conditions, unlike Si-enriched Type B CAI-like melts (CAIB, B133 and B113) which are charecterized by faster evaporation of Si compared to Mg.

Fig. 4. Chemical evaporation trajectories of experimental residues produced by evaporation of: (a, b) FoB-like CAI4B2 melt at low-pressure hydrogen and in vacuum at 1600°C (Table 1), and (c, d) Type B CAI-like CAIB melt evaporated in vacuum at 1600° to 1900°C (Richter et al., 2007). Evolution of evaporation residues is expressed as: (a, c) ratios of wt% MgO or SiO_2 over nonvolatile Al_2O_3 and normalized to the ratios in zero-time run, and (b, d) weight ratios of MgO/Al_2O_3 versus SiO_2/Al_2O_3. Also shown (open diamonds in panels a and b) are residues from evaporation of CAI4 melt (a different batch of CAI4B2) evaporated at 1900°C in vacuum. Arrows show direction in which composition of melts evolve during evaporation. The figure shows that silicon and magnesium evaporate from CAI4B2 melt at about the same ratio until near-complete evaporation of magnesium. Evaporation of silicon-enriched CAIB melt starts with faster loss of silicon compared to magnesium.

Fig. 5. Magnesium and silicon isotopic compositions in the CAI4B2 evaporation residues from vacuum (closed circles) and 2×10^{-4} bar H_2 experiments (closed diamonds). Labeled are samples from 2×10^{-4} bar H_2 experiment; also shown are the duration of the runs. The solid curve shows correlation of $\delta^{29}Si$ and $\delta^{25}Mg$ in vacuum and low-P_{H_2} CAI4B2 residues. Open symbols show isotopic compositions of CAIB residues (Mg data from

Richter et al., 2007, and Si data from Knight et al., 2009) which are characterized by much faster loss of Si relative to Mg at the initial stages (Fig. 4). Circled sample B2-10 contains large amount of melilite that was crystallized from the melt during the run. The bulk isotopic composition of B2-10 is a sum of isotopically lighter melilite and isotopically heavier melt that continued to evaporate (and fractionate isotopes) after melilite crystallization.

Fig. 6. Magnesium isotopic composition of CAI4B2 residues from vacuum and low-pressure H_2 experiments as a function of ^{24}Mg remaining in the melt. The linear dependence of $ln(R/R_0)$ versus $-ln\ f^{24}Mg$ confirms Rayleigh distillation (see Eqn. 7). The kinetic isotopic fractionation factor of ^{25}Mg relative to ^{24}Mg obtained from the slope of the best fitting line through all CAI4B2 data is $\alpha_{25,24} = 0.9877\pm0.0004$ ($\pm2\sigma$), which is the same as $\alpha_{25,24} = 0.98786\pm0.00032$ ($\pm2\sigma$) for vacuum experiments and $\alpha_{25,24} = 0.98745\pm0.00026$ ($\pm2\sigma$) for experiments at 2×10^{-4} bar H_2. Also shown are experimental data of Richter et al. (2007) for CAIB melt evaporated in vacuum at 1600°C (open circles) and data of Richter et al. (2002) for a BCAI melt evaporated at 2×10^{-4} bar H_2 at 1500°C (half-filled squares). The figure illustrates that magnesium isotopes fractionate in all these experiments the same way, independent of P_{H_2} of the surrounding gas and temperature. The analytical uncertainties are less than the symbol size. Circled sample B2-3 was not included in obtaining the regression line (see text for details).

Fig. 7. Temperature and melt composition effects on Mg isotopic fractionation factor $\alpha_{25,24}$ for melilitic and forsteritic melts. Also shown is the "ideal" value of $\alpha_{25.24} = \sqrt{24/25} = 0.97980$ expected if Mg evaporates as $Mg_{(g)}$. The isotopic composition data used are: FUN 1 and FUN2 from Mendybaev et al., 2013a,b; CAIB – from Richter et al., 2007; Mg_2SiO_4 – from Davis et al., 1990; solar – from Wang et al., 2001; B133 and BCAI – from Richter et al., 2002; CAI4B2 – from this work. To account for the isotopic fractionation during heating up the furnace to the experimental temperature (see text for details), the values of $\alpha_{25,24}$ were obtained using the least evaporated samples as a starting material in each set of experiments.

Fig. 8. Same as Fig. 6 but for silicon isotopes. The kinetic isotopic fractionation factor of ^{29}Si relative to ^{28}Si obtained from the slope of the best fitting line through both vacuum and low-P_{H_2} CAI4B2 evaporation residues is $\alpha_{29,28} = 0.9910\pm0.0005$. The value is the same as $\alpha_{29,28} = 0.9901\pm0.0005$ obtained using different composition melts at different temperatures (shown are FUN2 data at 1700°C and 1900°C from Mendybaev et al., 2013a,b, and CAIB data from Knight et al., 2009). The analytical uncertainties are less than the symbol size. Sample B2-3 (circled) was not included in obtaining the regression line.

Fig.9. Timescales required to deplete magnesium and silicon and to fractionate their isotopes in solar nebula gas with P_{H_2} of 2×10^{-4} and 2×10^{-5} bars at 1600° and 1500°C. The curves were calculated using chemical composition of a 2.5-mm diameter CAI4B2 droplet and experimental evaporation rates at 1600°C from this study and those at 1500°C and 2×10^{-4} bar H_2 from Richter et al. (2002). Typical fractions of magnesium and silicon evaporated and $\delta^{25}Mg$ and $\delta^{29}Si$ values in coarse-grained Type A and B CAIs are from

Grossman et al. (2000) and those for the most fractionated FUN and Type F CAIs are from Fig. 12 of Mendybaev et al. (2017).